

# 1 Measurements of frazil ice flocs in rivers

2 Chuankang Pei<sup>1</sup>, Jiaqi Yang<sup>1</sup>, Yuntong She<sup>1</sup>, Mark Loewen<sup>1</sup>

3 <sup>1</sup>Department of Civil and Environmental Engineering, University of Alberta, Edmonton, AB, T6G 1H9, Canada

4 *Correspondence to:* Mark Loewen (mrloewen@ualberta.ca)

5 **Abstract.** Frazil floc sizes and concentrations have been investigated in a small number of laboratory studies but no detailed  
6 field measurements have been reported previously. In this study, a submersible camera system was deployed a total of eleven  
7 times during the principal and residual supercooling phases in the North Saskatchewan, Peace, and Kananaskis Rivers to  
8 capture time-series images of frazil ice particles and flocs. Images were processed to accurately identify flocs and to calculate  
9 their sizes and concentrations. Key hydraulic and meteorological measurements were collected and air-water heat fluxes were  
10 estimated to investigate their influence on floc properties. A lognormal distribution was found to be a good fit for the floc size  
11 distribution. The mean floc size ranged from 1.19 to 5.64 mm and the overall mean floc size was 3.80 mm. The mean floc size  
12 decreased linearly as the local Reynolds number increased. The average floc number concentration ranged from  $1.80 \times 10^{-4}$  to  
13  $1.15 \times 10^{-1} \text{ cm}^{-3}$ . The average floc volumetric concentration ranged from  $2.05 \times 10^{-7}$  to  $4.56 \times 10^{-3}$  and was found to correlate  
14 strongly with the ~~relative depth of fractional height above the measurements river bed~~. No significant correlations were found  
15 between the air-water heat flux and floc properties. Time series analysis showed that during the principal supercooling phase,  
16 floc number concentration and mean size increased significantly just prior to peak supercooling and reached a maximum near  
17 the end of principal supercooling. During the residual supercooling phase, the mean floc size did not typically vary significantly  
18 even 2.5 hours after the residual phase ended and the water temperature increased above zero degrees.

## 19 1 Introduction

20 In northern rivers, individual frazil ice particles form when the water is turbulent and supercooled below its freezing point due  
21 to heat loss to the atmosphere. These suspended particles are ice crystals that are inherently adhesive in the supercooled water.  
22 As they are transported by the turbulent flow, they ~~can~~ may collide with each other due to spatially varying particle velocities  
23 resulting from differential rising or due to spatially varying flow velocities created by turbulent eddies and ~~sinter~~ boundary  
24 shear (Mercier, 1985). Colliding particles may freeze together ~~into~~ forming clusters of particles known as frazil flocs in a  
25 process called flocculation (Clark and Doering, 2009). Frazil flocs grow increase in size either by the thermal growth of the  
26 crystals and/or by further aggregation of individual frazil ice particles or flocs. Once frazil flocs grow into a sufficiently  
27 buoyant mass gain sufficient buoyancy they rise to the water surface forming surface ice pans or are deposited under existing  
28 surface ice contributing to their mass growth increase (Hicks, 2016). In addition, turbulent flow may transport flocs to the river  
29 bed where they may adhere to the bed forming anchor ice (Kempema et al., 1993). Once the surface ice pan concentration is

30 high enough, congestion of incoming ice pans will occur at certain locations where there is a flow constriction and a solid ice  
31 cover will form and propagate upstream (Beltaos, 2013). The formation of a continuous solid ice cover insulates the flowing  
32 water from further heat loss to the atmosphere, thus preventing the occurrence of supercooling and the production of frazil ice  
33 until the ice cover thaws or breaks up (Beltaos, 2013). Frazil flocs may cause serious problems at hydroelectric facilities and  
34 water treatment plants by adhering to water intake, trash racks and partially or fully blocking the flow (Ettema and Zabilansky,  
35 2004; Barrette, 2021, Ghobrial et al., 2024). Therefore, it is important to obtain a better understanding of the properties of  
36 frazil flocs as well as their evolution to better model and predict their behavior.

37

38 As the constructing unit of frazil flocs, individual frazil ice particles have been investigated both in laboratory settings and  
39 field. These particles exhibit various forms including dendritic, needle, and irregular but are predominately disc-shaped with  
40 diameters ranging from 0.022 to 6 mm (McFarlane et al., 2017) and diameter-to-thickness ratios of 11 to 71 (McFarlane et al.,  
41 2014). A lognormal distribution can be used to describe the particle size distribution (Daly and Colbeck, 1986; Clark and  
42 Doering, 2006; McFarlane et al., 2015). During the principal supercooling period when the water temperature varies  
43 transiently, the time from the start of supercooling to when a steady residual supercooling water temperature is reached, the  
44 mean diameter of particles was found to first increase before reaching an approximately constant value (Clark and Doering,  
45 2006; McFarlane et al., 2015). At the same time the number concentration of suspended particles first increased slowly then  
46 more rapidly, peaking just after peak supercooling occurred (i.e., the minimum water temperature) (McFarlane et al., 2015;  
47 Ye, 2002; Clark and Doering, 2006). The rapid increase in particle concentration was attributed to secondary nucleation which  
48 refers to the formation of new crystals due to the presence of stable parent crystals (Evans, et al., 1974). After peaking the  
49 particle concentration decreased as particles were removed via flocculation.

50

51 There have been a small number of laboratory studies that investigated the properties of frazil flocs as well as the flocculation  
52 process. Park and Gerard (1984) used artificial flocs fabricated from plastic discs to investigate the hydraulic characteristics  
53 of frazil flocs. They found that the sharp-edged floc surface resulted in a significantly higher drag coefficient compared to a  
54 solid smooth sphere of the same size and density. Kempema et al. (1993) conducted racetrack flume experiments to investigate  
55 interactions of frazil and anchor ice with sediments. They observed that in freshwater frazil easily agglomerated into roughly  
56 spherical flocs up to 8 cm in diameter. Flocs that struck the bed tended to entrain sediments into their voids and become heavy  
57 and settle to the bottom in the shelter of ripples forming anchor ice. Reimnitz et al. (1993) observed the characteristics and  
58 behaviour of rising frazil in seawater using a stirred vertical tube or tank. They found that individual frazil crystals combine  
59 rapidly into flocs with diameters as large as 5 cm. The rise velocities of flocs ranged from 1 to 5 cm s<sup>-1</sup> and rapidly rising large  
60 flocs induced small-scale turbulence. The porosities of the resulting surface slush accumulations ranged from 0.68 to 0.85,  
61 with an average of 0.77. Clark and Doering (2009) investigated frazil flocculation under different turbulence intensities using  
62 a counter-rotating flume. Results showed that higher levels of turbulence increased the rate of secondary nucleation, inhibited  
63 the formation of large flocs, and produced more dense flocs.

64

65 Schneck et al. (2019) measured the size and number concentration of frazil ice particles and flocs in water of varying salinity  
66 using a stirred frazil ice tank. Results showed that the mean floc size was 2.57 mm in freshwater and 1.47 mm in saline water  
67 and a lognormal distribution fit the floc size distributions closely. The floc porosity was estimated to vary from 0.75 to 0.86.  
68 Time series measurements of floc properties indicated that, in freshwater, the floc number concentration and mean size started  
69 to increase significantly just prior to peak supercooling, reached a maximum shortly afterwards. After that floc number  
70 concentration decreased slowly while the mean floc size continually increased very slowly during the principal supercooling  
71 period.

72

73 The above studies were all conducted in laboratory facilities that do not replicate the complex natural environment.  
74 Measurements of frazil flocs in supercooled rivers are needed to verify the laboratory results and improve numerical river ice  
75 process models. However, no detailed quantitative field measurements of the properties or evolution of frazil flocs have been  
76 reported in the literature. The objective of this study was to determine the statistical characteristics and temporal evolution of  
77 floc sizes and concentrations, as well as to investigate the key factors affecting the properties of frazil flocs in rivers. A  
78 submersible high-resolution camera system was used to capture time-series images of frazil flocs. Images were analyzed to  
79 accurately determine floc sizes and concentrations. Key hydraulic and meteorological measurements were collected and air-  
80 water heat fluxes were estimated to investigate their influence on floc properties. Time series of floc size, number concentration  
81 and volumetric concentrations as well as size distributions measured in rivers during the principal and residual supercooling  
82 phase are presented for the first time.

## 83 **2 Study Reaches**

84 Measurements were conducted in three regulated Alberta rivers, the North Saskatchewan River (NSR) at Edmonton, the Peace  
85 River (PR) near Fairview, and the Kananaskis River (KR). Figure 1 shows the geographical locations of the study reaches,  
86 deployment sites and weather stations. The characteristics of the study reaches are summarized in Table 1. The turbulent  
87 dissipation rate in Table 1 was estimated using the listed slope as well as the average depth and width following Clark and  
88 Doering (2008). The three rivers are significantly different in terms of their size and hydraulic characteristics. The flow of the  
89 NSR is regulated by the Brazeau and Bighorn Dams which are ~233 km and ~423 km upstream of the Laurier Park site,  
90 respectively. A daily water level fluctuation of 0.3 to 0.4 m occurred in the study reach due to hydropeaking (McFarlane et al.,  
91 2017). The estimated turbulence dissipation rate is  $0.0058 \text{ m}^2 \text{ s}^{-3}$ . Freeze-up typically starts in early November and ends in  
92 early to late December with the formation of a static ice cover. However, the 2022 winter freeze-up progressed in a surprisingly  
93 rapid manner, starting on Nov 5, 2022, and ending just three days later on Nov 8, 2022.

94

95 PR has the largest average discharge, depth, and width of the three rivers (Table 1). The estimated turbulence dissipation rate  
 96 is 0.0051 m<sup>2</sup> s<sup>-3</sup> which is slightly smaller than NSR. The flow of PR is regulated by the W.A.C Bennett Dam and the Peace  
 97 Canyon Dam which are ~309 km and ~ 288 km upstream of the Fairview water intake deployment site, respectively. These  
 98 outflows at the dams are relatively warm water (~6 °C) during the winter, affecting the river thermal regime for up to 550 km  
 99 downstream of the dams (Jasek and Pryse-Phillips, 2015) which is ~250 km downstream of the deployment site. Therefore,  
 100 supercooling and frazil ice generation only occurs at the deployment site when the zero-degree isotherm is located upstream  
 101 and ceases when it retreats downstream. This unique condition allows freeze-up to persist until the ice front reaches the  
 102 Fairview intake site typically in mid-January.

103

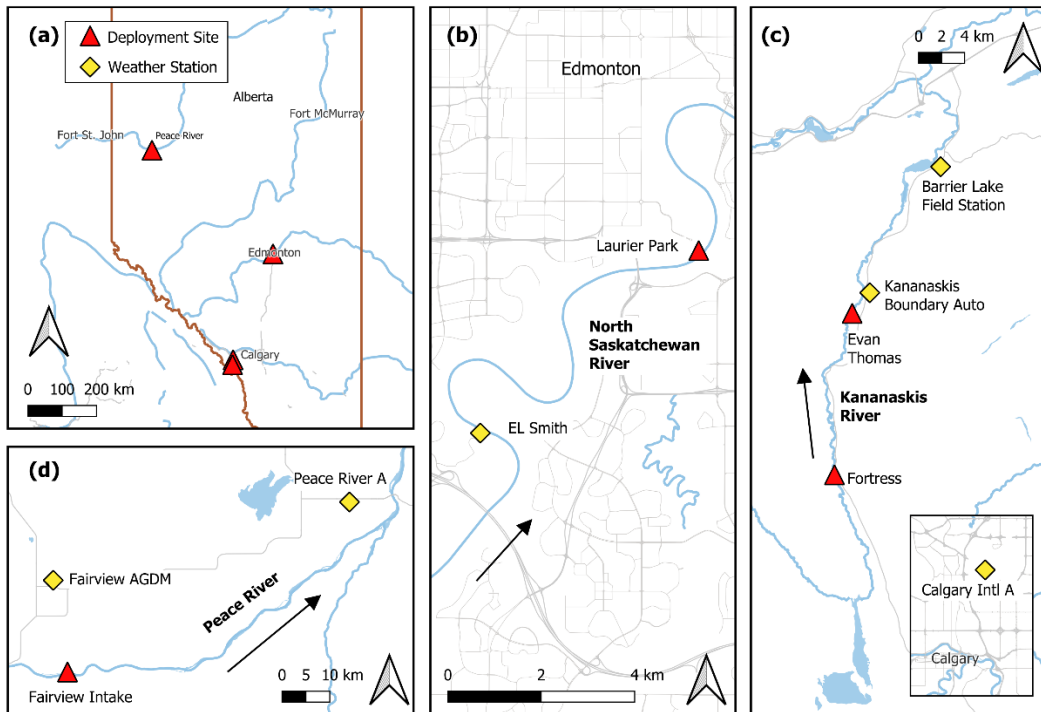
104 KR is the smallest of the three rivers in terms of average discharge, depth, and width (Table 1). It has the largest turbulence  
 105 dissipation rate with a value of 0.2066 m<sup>2</sup> s<sup>-3</sup>, which is not unexpected since KR is a small-steep river in the mountains. The  
 106 flow is regulated by the Pocaterra Dam which is 12 and 31 km upstream of the Fortress and Evan Thomas deployment sites,  
 107 respectively. In winter, a dramatic discharge fluctuation from ~1 m<sup>3</sup> s<sup>-1</sup> to 21 m<sup>3</sup> s<sup>-1</sup> occurred daily in the study reach due to  
 108 hydropeaking (Government of Alberta, 2023). Low flows promote border ice formation reducing channel width, while high  
 109 flows cause overtopping of existing ice and/or banks and prevent the formation of a complete ice cover. Without an ice cover  
 110 to insulate the water, supercooling events and frazil generation occur when the air temperature is sufficiently cold.

111

112 **Table 1: Summary of the study reach characteristics.**

River	Slope	Average discharge (m <sup>3</sup> s <sup>-1</sup> )	Average depth (m)	Average width (m)	Average $D_{100}$ of suspended sediment (mm)	<u>Estimated turbulence dissipation rate (m<sup>2</sup> s<sup>-3</sup>)</u>
NSR	0.00035	220	1.40	136	0.50	<u>0.0058</u>
PR	0.00025	1586	2.56	227	0.68	<u>0.0051</u>
KR	0.005	15	0.61	32	N/A	<u>0.2066</u>

113 *Note:* Slope, average discharge, average depth, and average width were obtained from Kellerhals et al. (1972); Average  $D_{100}$   
 114 of suspended sediments were computed from Water Survey of Canada historic size distribution data measured at North  
 115 Saskatchewan River at Edmonton (05DF001) and Peace River at Dunvegan Bridge (07FD003) (Water Survey of Canada,  
 116 2023).



117

118 **Figure 1: Maps showing (a) the locations of the deployment sites in Alberta, enlarged views of the locations on (b) the North**  
 119 **Saskatchewan, (c) Kananaskis, and (d) Peace rivers.**

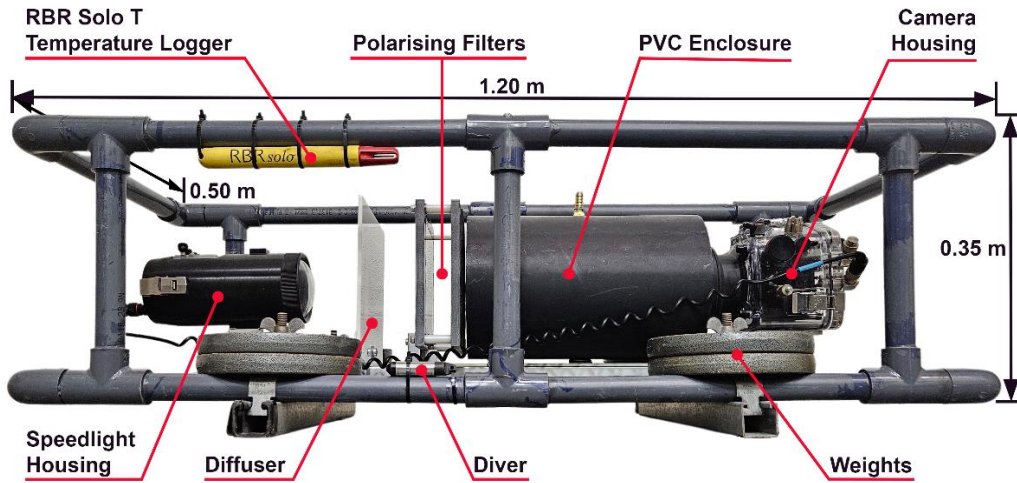
### 120 3 Instrumentation, Methodology and Deployments

121 A submersible camera system initially designed for imaging suspended frazil ice particles named “FrazilCam” (McFarlane et  
 122 al., 2017) was modified in this study to ~~capture image~~ frazil flocs in the water column. Figure 2 shows the modified  
 123 configuration of the FrazilCam system. A 36-megapixel Nikon D800 DSLR camera equipped with a Micro-Nikkor 60 mm  
 124 f/2.8D lens was used to image underwater frazil ice particles and flocs. The camera was enclosed in an Ikelite waterproof  
 125 housing. Two 16 cm × 16 cm Cavisson linear glass cross-polarizing filters were mounted 3.6 cm apart ~~to enable clear imaging~~  
 126 ~~of frazil ice particles and flocs as they advected between the polarizers., which is 1.6 times larger than the original~~  
 127 ~~configuration.~~ A PVC enclosure with a brass fitting on the top was installed in between the camera lens and polarizing filters  
 128 to prevent ice or debris from flowing through this region blocking the camera field-of-view (FOV). The brass fitting was used  
 129 for hot water injection to melt any ice that was initially trapped inside the enclosure. A Nikon SB-910 Speedlight flash in a  
 130 Subal SN-910 waterproof housing was used as the light source, and a 5 mm thick white acrylic board was placed in between  
 131 the polarizers and flash to diffuse the light. ~~The modified configuration resulted in ~6 times bigger FOV and 1.6 times larger~~  
 132 ~~gap compared to McFarlane et al. (2017), enabling larger flocs to pass through and fit in the FOV.~~ The camera settings were  
 133 determined by submerging the system in a laboratory tank filled with tap water and capturing images of a transparent plastic

134 ruler placed inside the camera FOV. This yielded an ISO of 6400, aperture f/25, and a shutter speed of 1/320. The configuration  
135 resulted in an image scale of  $25.6 \mu\text{m}$  per pixel and an average FOV of 11.6 cm by 15.6 cm— which is 6 times larger than the  
136 original configuration. The reason for enlarging the FOV and increasing the gap between the polarizers was to enable larger  
137 flocs to pass through and fit within the FOV.

138  
139 At the start of each deployment, the camera was programmed to acquire 5 images at 1 Hz every 9 s, 15 s, or ~~1918~~ s depending  
140 on the field conditions until the battery was depleted. A longer sampling interval (e.g. ~~1918~~ s) was chosen for some  
141 deployments to prolong the deployment duration with the goal of capturing a complete supercooling event. Just prior to  
142 deployment of the FrazilCam in the river, the polarizers were rinsed with hot saline water to prevent ice crystals from forming  
143 on them once submerged. The system was then quickly deployed in the river and the PVC enclosure was filled with hot fresh  
144 water from an elevated container. During deployments, anchor ice often formed on system components as shown in Fig. 3 and  
145 ice that formed on the polarizers could obstruct the FOV of the camera. To prevent or mitigate this problem, the polarizers  
146 were inspected every 30 to 60 minutes and hot saline water was injected onto the polarizers to melt any ice crystals.

147  
148 During each deployment, an RBR Solo T (accuracy  $\pm 0.002^\circ\text{C}$ ) temperature logger sampling every second was attached to the  
149 top of the frame to measure water temperature, and a Van Essen Diver (accuracy  $\pm 1 \text{ cmH}_2\text{O}$ ) water level logger sampling  
150 every 10 minutes was attached to the bottom of the frame to measure the water depth (Fig. 2). The water depth during the PR  
151 deployments was measured using a wading rod since the Diver stopped working at that time. ~~Depth~~For all deployments the  
152 depth-averaged water velocity was estimated using velocities measured adjacent to FrazilCam at 60% of the water depth.  
153 During the 2021 winter, the ~~depth-averaged~~-water velocity was measured using a ~~2-MHz~~ Nortek ~~Aquadop~~acoustic~~AquaDopp~~  
154 High Resolution Acoustic Doppler ~~current profiler (ADCP)~~Current Profiler sampling every second with a blanking distance  
155 of 0.1 m and averaging every two minutes. For the rest of the deployments, the ~~depth-averaged~~-water velocity was measured  
156 using a SonTek Flow Tracker ~~handheld acoustic~~Handheld Acoustic Doppler ~~velocimeter~~Velocimeter (ADV) sampling every  
157 second for a total duration of 50 seconds.



158

159 **Figure 2: An image showing the configuration of the FrazilCam system.**



160

161 **Figure 3: An image showing the ice accumulation on the FrazilCam system.**

162 Meteorological conditions for the NSR reach were measured by a weather station installed at the E.L. Smith water treatment  
 163 plant, which is located ~90 m from the river bank and ~6 km upstream of Laurier Park site (Fig. 1b). The weather station  
 164 measures the air temperature, solar radiation, relative humidity, atmospheric pressure, wind speed and direction every minute  
 165 and logs data every 10 minutes. An Apogee SN-500-SS net radiometer was deployed on the river bank at this location,  
 166 measuring incoming and outgoing shortwave/longwave radiation every minute and logging data every 10 minutes. For the PR,  
 167 1-hour interval meteorological data were obtained from ECCC station Fairview AGDM (ID: 3072525) and 3-hour interval  
 168 cloud coverage data was obtained from the closest ECCC station Peace River A (ID: 3075041) as shown in Fig. 1d. For the  
 169 KR, the Kananaskis Boundary Auto weather station operated by Alberta Forestry, Parks and Tourism (ACIS, 2023) was used  
 170 to obtain 1-hour interval air temperature, humidity, wind speed, and wind direction data. In addition, 1-hour solar radiation

171 data was obtained from the University of Calgary Barrier Lake Field Station weather station (University of Calgary, 2023),  
 172 and 3-hour cloud coverage data was obtained from the closest ECCC station Calgary Intl A (ID: 3031092) as shown in Fig.  
 173 1c. Table 2 summarizes the distance between weather stations and deployment sites. All weather stations are located within  
 174 30 km of their nearby deployment sites, except for those providing cloud coverage data for PR and KR.

175

176 **Table 2: The distances between weather stations and deployment sites.**

River	Deployment site	Distance - weather station
NSR	Laurier Park	6 km - E.L. Smith
PR	Fairview Intake	18 km - Fairview AGDM; 68 km - Peace River A
	Evan Thomas	2 km - Kananaskis Boundary Auto; 15 km - Barrier Lake Field Station; 82 km - Calgary Intl A
KR		A
	Fortress	16 km - Kananaskis Boundary Auto; 28 km - Barrier Lake Field Station; 88 km - Calgary Intl A

177

178 The FrazilCam system was deployed a total of eleven times during the 2021 and 2022 ~~freezeup~~freeze-up periods, images of  
 179 the FrazilCam during two of the deployments are shown in Fig. 4-4. The image sampling protocols were 5 images at 1 Hz  
 180 every 9 s for all NSR and KR-E1 deployments, for KR-F1 and KR-F2 5 images at 1 Hz every 15 s, and for all PR deployments  
 181 5 images at 1 Hz every 18 s. Table 3 lists the detailed location, date, time, number of images processed, and deployment  
 182 number for each deployment. The mean air temperature  $\bar{T}_a$ , mean water depth  $\bar{d}$ , depth-averaged flow velocity  $\bar{U}$ , and the local  
 183 Reynolds number  $Re$  computed from  $\bar{d}$  and  $\bar{U}$  are also presented in Table 3. Eight of eleven deployments started in the  
 184 afternoon around 2 PM ~ 7 PM when the effect of solar radiation reduced decreasing heat gain of the water body, the time  
 185 duration of deployments ranged from 1:48 to 3:21. As can be seen from Table 3, during these deployments  $\bar{T}_a$  ranged from -  
 186 3.5 °C to -20.6 °C,  $\bar{d}$  ranged from 0.41 m to 1.24 m,  $\bar{U}$  ranged from 0.12 m s<sup>-1</sup> to 0.36 m s<sup>-1</sup>, and  $Re$  ranged from 44866 to  
 187 160714, respectively, indicating that frazil floc properties and concentrations were measured and analyzed over a wide range  
 188 of meteorological and hydraulic conditions. The eleven deployments captured various phases of supercooling but NSR-L4 was  
 189 the only deployment that captured a complete principal supercooling phase (i.e., from when the water temperature first dropped  
 190 below zero to when an approximately stable residual temperature was reached).

191

192

193

194

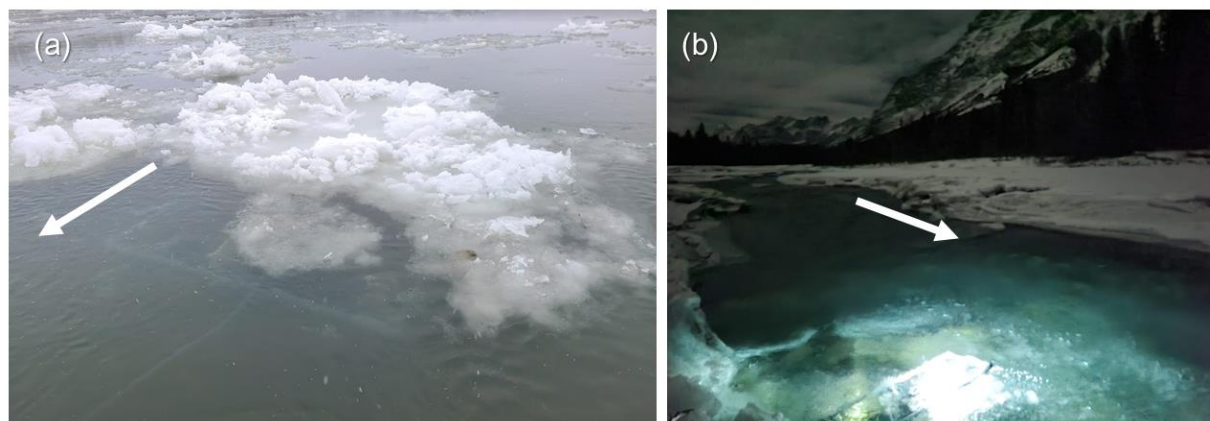
195

196

197 Table 3: Summary of the FrazilCam deployments and site conditions including the number (#) of images captured, mean air  
 198 temperature  $\bar{T}_a$ , mean water depth  $\bar{d}$ , depth averaged water velocity  $\bar{U}$ , and local Reynolds number  $Re$ .

River	Date (yyyy.mm. dd)	Time period (hh:mm~hh: mm)	Time duration (hh:mm)# of processed images	Site	Deployment No.	$\bar{T}_a$ (°C)	$\bar{d}$ (m)	$\bar{U}$ (m s <sup>-1</sup> )	$Re$
NSR	2021.12.3	16:41~18:49	<del>2:084,099</del>	Laurier Park	NSR-L1	-7.2	0.89	0.21	104,297
		19:05~21:34	<del>2:294,797</del>	Laurier Park	NSR-L2	-10.5	0.84	0.17	79,688
	2021.12.9	14:46~17:09	<del>2:234,688</del>	Laurier Park	NSR-L3	-3.5	1.24	0.19	131,473
	2021.12.12	15:02~16:50	<del>1:483,495</del>	Laurier Park	NSR-L4	-4.6	0.87	0.22	106,808
		17:08~19:31	<del>2:234,091</del>	Laurier Park	NSR-L5	-9.2	0.86	0.20	95,982
	2022.11.7	14:31~16:22	<del>1:513,596</del>	Laurier Park	NSR-L6	-12.1	0.80	0.36	160,714
PR	2022.12.12	10:40~13:57	<del>3:47,155</del>	Fairview Intake	PR-F1	-20.6	0.82	0.30	137,277
	2022.12.13	9:41~13:02	<del>3:21,208</del>	Fairview Intake	PR-F2	-6.0	0.74	0.23	94,978
KR	2023.1.29	18:00~20:02	<del>2:023,728</del>	Evan Thomas	KR-E1	-15.8	0.41	0.22	50,335
	2023.1.30	14:46~17:59	<del>3:43,379</del>	Fortress	KR-F1	-11.1	0.55	0.30	92,076
	2023.1.31	7:28~10:39	<del>3:44,610</del>	Fortress	KR-F2	-13.3	0.67	0.12	44,866

199



200

201 Figure 4: Image of the FrazilCam deployed during (a) NSR-L6, and (b) KR-E1. The arrow indicates the flow direction.

## 202 4 Data processing

### 203 4.1 Image processing

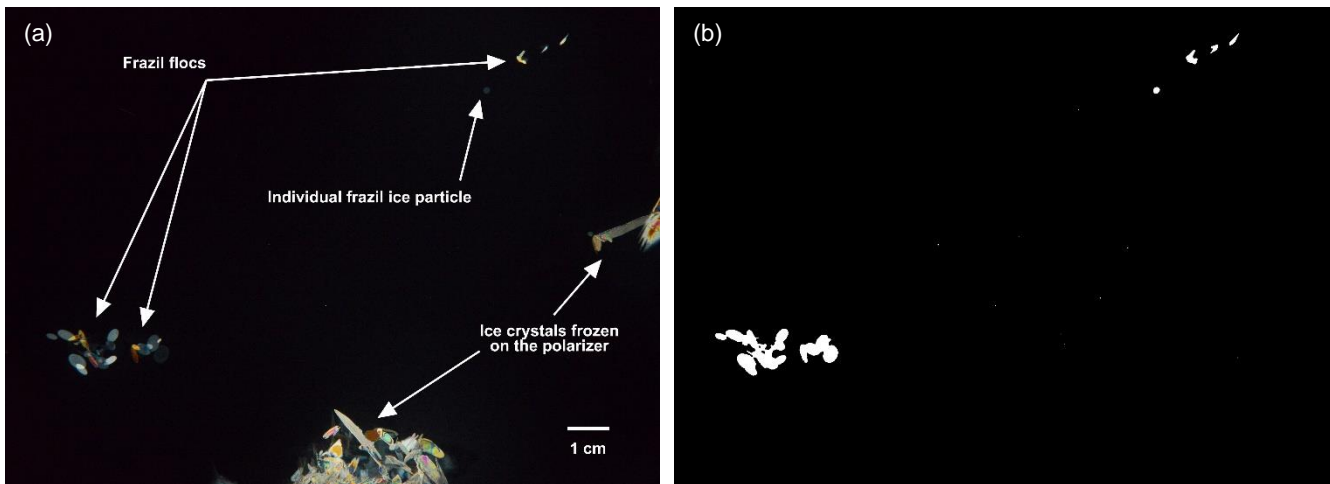
204 Figure 5a shows an example of a raw FrazilCam image with individual frazil ice particles, flocs, and ice crystals frozen on the  
205 polarizer. Frazil ice particles are predominantly disk-shaped (McFarlane et al., 2017) and therefore depending on their  
206 orientation appear in the images as shapes that vary from a line to a circle with the majority being ellipses. Flocs form through  
207 the aggregation of frazil ice particles, resulting in varying shapes depending on the number, shape, and size of attached  
208 particles. Ice crystals sometimes attached and froze to the surface of the polarizers despite the periodic hot saline water rinsing.  
209 These crystals may appear anywhere in the image, blocking certain regions of the FOV.

210

211 Figure 6 shows a flow chart of the image processing procedure used for extracting frazil floc properties. For each deployment,  
212 images were first manually inspected to exclude those taken when the polarizers were being rinsed-, which constitutes 2 ~ 14%  
213 of the total images captured. Each image was then processed using an iterative thresholding algorithm developed by McFarlane  
214 et al. (2014) to determine the location and extent of each object. Objects intersecting with the image boundary were eliminated,  
215 which also removed the ice crystals that were frozen near polarizer edges. For frozen ice crystals that did not intersect with the  
216 image boundary, the affected image area was removed either by cropping or masking, or a combination of both- (Fig. 6). The  
217 corresponding processed binary image is shown in Fig. 5b.

218

219 **Figure 5: An example of (a) a raw FrazilCam image captured on Dec 3, 2021, and (b) the corresponding processed binary image.**



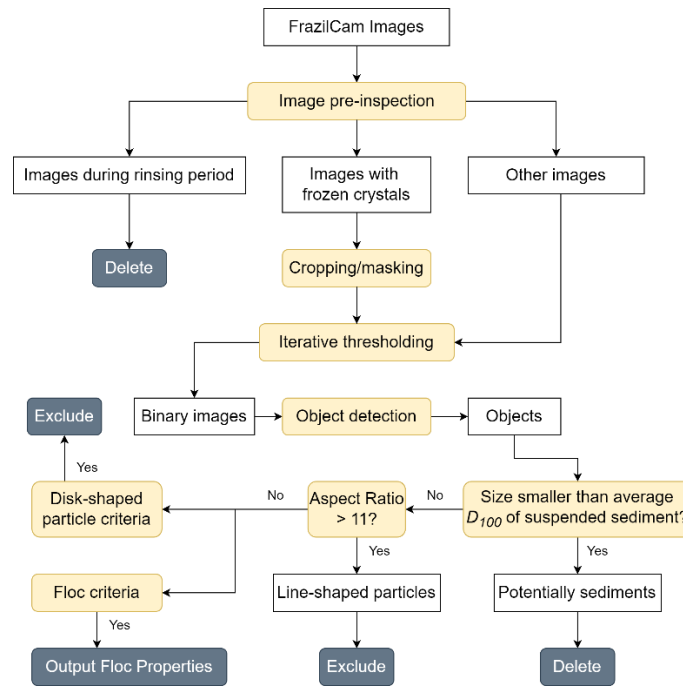


**Figure 6: A flow chart showing the image processing procedure.**

The processed binary images were analyzed to compute each object's basic geometric characteristics such as area, perimeter, centroid, as well as the major and minor axis length of its fitted ellipse. The size  $S$  of both frazil particles and flocs was defined as the major axis length of its fitted ellipse (Clark and Doering, 2009). The objects in the processed images may include small-suspended sediments that were thin enough to refract light, which may significantly distort the size distribution of frazil ice particles and flocs (McFarlane et al., 2017; Pei et al., 2022). McFarlane et al. (2019a) used a support vector machine (SVM) to distinguish between ice particles and sediments and compute accurate particle size distributions. However, this method requires ice-free sediment images at each site for site-specific SVM training, which is not possible for this study due to the lack of ice-free images at the PR and KR sites. Since this study focuses on flocs, which are considerably larger than particles, a simple cut-off criterion was used to minimize the effect of sediment particles in the images. Objects smaller than the average  $D_{100}$  of suspended sediment (see Table 1) in a given study reach were removed from the dataset- (Fig. 6). For the KR, since no suspended sediment size distribution measurements were available in the literature, the cut-off size was determined to be 0.27 mm, which is twice the average of seven mean sediment size measurements estimated from FrazilCam images by McFarlane et al. (2019b).

For each object, the following geometric parameters were used to classify the objects into either flocs or particles: the ratio of the object area to that of the fitted ellipse  $a/a_e$ , the absolute percentage difference between the object perimeter and its fitted

239 ellipse perimeter  $P_{diff\%}$ , the ratio of an object's fitted ellipse area to its ellipse perimeter divided by the ratio of the object's  
 240 actual area to its perimeter  $(\frac{a_e}{p_e})/(\frac{a}{p})$  (McFarlane et al., 2014; Schneck, 2018). Preliminary experiments found that flocs formed  
 241 by a very small particle attaching to a significantly larger particle remain approximately elliptical since the boundary does not  
 242 change significantly. As a result, comparing changes in overall area/perimeter with the fitted ellipse did not help with  
 243 classification. Therefore, the form index was introduced to assess minor changes in object shape (Masad et al., 2001; Al-  
 244 Rousan et al., 2007). The form index is calculated using the following equation:

$$245 \quad FI = \sum_{\theta=0}^{\theta=360-\Delta\theta} \frac{|R_{\theta+\Delta\theta}-R_{\theta}|}{R_{\theta}}, \quad (1)$$

246 where  $\theta$  is the directional angle and  $R$  is the radial length between the centroid of the particle and the boundary of the particle.  
 247 The incremental change in angle  $\Delta\theta$  is set to  $2.81^\circ$ , dividing the particle boundary into 128 segments to factor in minor  
 248 boundary changes. A perfectly circular object has an  $FI$  of 0, and  $FI$  will increase as an object's boundary becomes more  
 249 irregular.

250

251 A total of 568 objects were manually labelled as either flocs (109) or disk-shaped frazil particles (459) to construct a test  
 252 dataset to determine the optimal classification criteria of the aforementioned parameters. Results showed that  
 253  $\{a/a_e \geq 0.9 \text{ and } P_{diff\%} \leq 0.1 \text{ and } S \leq 6\}$  for disk-shaped particles, and  $\{(a/a_e < 0.9 \text{ or } P_{diff\%} > 0.15) \text{ and } (\frac{a_e}{p_e})/$   
 254  $(\frac{a}{p}) \frac{a_e p_e}{a p} > 1.1 \text{ and } FI \geq 6\}$  for flocs provided the optimum classification accuracy of 97.0% and 92.7% for particles and  
 255 flocs, respectively. In NSR-L4 the camera lens was slightly out of focus due to an accidental jarring of the camera during  
 256 deployment. However, because this was the only deployment that captured a complete principal supercooling event, additional  
 257 processing was performed on these images to allow for their inclusion in the dataset. Visual examination and analysis of these  
 258 images indicated that the blurriness predominantly affected the boundary clarity of dim objects with a mean pixel intensity  
 259 less than 24 and did not significantly affect brighter objects. Therefore, an additional criterion was introduced for NSR-L4  
 260 eliminating flocs with a mean pixel intensity less than 24. The rate of floc detection in the blurry images from deployment  
 261 NSR-L4 was 4.1 flocs per minute and it was 4.4 flocs per minute in NSR-L5 which occurred immediately afterwards.  
 262 Therefore, the additional criterion, applied to the blurry images, only slightly reduced the number of flocs detected.

263

264 In order to prevent line-shaped frazil ice particles from being misidentified as flocs, frazil particles in the shape of a line were  
 265 first identified if the aspect ratio of the object (i.e., the ratio between the major and minor axis length) was greater than 11  
 266 based on minimum frazil ice particle aspect ratio measurements made by McFarlane et al. (2014) as shown in Fig. 6. Then  
 267 the classification criteria mentioned above were applied to the remaining objects to identify disk-shaped particles and flocs-  
 268 (Fig. 6). After classification, the number of flocs  $N_T$ , mean floc size  $\overline{\mu_f}$ , standard deviation  $\sigma_f$ , 95<sup>th</sup> percentile of floc size  $S_{95}$ ,  
 269 maximum floc size  $S_{fmax}$ , average floc number concentration  $\overline{C_{fn}}$ , and average volumetric concentration  $\overline{C_{fv}}$  for each

270 deployment were computed. It is worth noting that the properties of frazil ice particles were not included in this study since  
 271 the cut-off size likely eliminated up to 50% of the particle population which would significantly skew the data. In addition, the  
 272 mean floc size  $\mu_f$ , floc number concentration  $C_{fn}$ , floc volumetric concentration  $C_{fv}$  were computed for each image throughout  
 273 a deployment, and a moving average over a period of 35 images was applied to the resulting time series to smooth the data.  
 274 Note that the 35-image moving average was computed only if two or more non-zero values occurred in the window, if there  
 275 were less than two non-zero values no average value was recorded. This created gaps in the moving average time series and  
 276 the rationale for this is that two or more samples are required to compute a valid average value. The measuring volume used  
 277 for the concentration calculations was the image FOV times the gap distance between the two polarizers. The volume of a  
 278 frazil floc was assumed to be the volume of an ellipsoid with semi-axis lengths  $a$ ,  $b$ , and  $c$  where  $a$  and  $b$  were equal to the  
 279 semi-major and semi-minor axis lengths of the floc's fitted ellipse, and  $c$  was equal to the average of  $a$  and  $b$  but no larger than  
 280 the gap between the two polarizing filters. The volume of ice in a frazil floc  $V_f$  was estimated as:

$$281 \quad V_f = \frac{4}{3} \pi abc(1 - \eta) , \quad (2)$$

282 where  $\eta$  is the porosity of floc taken to be 0.8 (Schneck et al., 2019).

## 283 **4.2 Heat flux analysis at the water surface**

284 The net heat flux  $Q_n$  at the river surface ~~can be expressed as~~ given by:

$$285 \quad Q_n = Q_{sw} + Q_{lw} + Q_E + Q_H , \quad (3)$$

286 where  $Q_{sw}$  is the net shortwave radiation;  $Q_{lw}$  is the net longwave radiation;  $Q_E$  is the latent heat flux;  $Q_H$  is the sensible heat  
 287 flux. A positive sign denotes heat loss from the surface.  $Q_{sw}$  ~~can be~~ was calculated as:

$$288 \quad Q_{sw} = -(1 - \alpha_{ws})Q_s , \quad (4)$$

289 where  $Q_s$  is the measured incoming solar radiation;  $\alpha_{ws}$  is the albedo of water surface to solar radiation, taken to be 0.15 for  
 290 this study following Howley (2021). The net longwave radiation  $Q_{lw}$  ~~can be~~ was calculated as:

$$291 \quad Q_{lw} = Q_{lw}^{out} - (1 - \alpha_{wl})Q_{lw}^{in} , \quad (5)$$

$$292 \quad Q_{lw}^{out} = \varepsilon_w \sigma_{sb} T_{wk}^4 , \quad (6)$$

293 where  $Q_{lw}^{out}$  is the outgoing longwave radiation emitted from the water;  $\alpha_{wl}$  is the albedo of water surface to longwave  
 294 radiation, taken as 0.03 (Raphael, 1962);  $\varepsilon_w$  is the emissivity of water taken as 0.97 (Ashton, 2013);  $\sigma_{sb}$  is the Stefan-  
 295 Boltzmann constant ( $5.67 \times 10^{-8} \text{ W m}^{-2} \text{ K}^{-4}$ );  $T_{wk}$  is the water ~~temperature in K~~ surface temperature in K. Note that it was  
 296 assumed that the water column was completely mixed and therefore the water temperatures that were measured at the top of  
 297 the FrazilCam frame (i.e., not at the water surface) were used in Eq. (6).  $Q_{lw}^{in}$  is the incoming longwave radiation which was  
 298 measured by a net radiometer for the NSR. For KR and PR,  $Q_{lw}^{in}$  ~~is estimated using the Satterlund (1979) equation for clear sky~~

299 conditions and Konzelmann et al. (1994) equation for cloudy conditions following a method described by Yang et al. (2023).  
 300 For the remaining heat fluxes,  $Q_E$  can be calculated using the equation suggested by Ryan et al. (1974), and  $Q_H$  can be  
 301 calculated from  $Q_E$  using Bowen's ratio.  $B$  is estimated using the following equations:

$$302 \quad Q_{lw\_c}^{in} = \varepsilon_{ac} \sigma_{sb} T_{ak}^4 \quad (7)$$

$$303 \quad \varepsilon_{ac} = 1.08[1 - \exp(-e_a^{T_{ak}/2016})] \quad (8)$$

$$304 \quad e_s = 6.11 \exp\left(\frac{17.62T_a}{243.12+T_a}\right) \quad (9)$$

$$305 \quad e_a = RH \times e_s \quad (10)$$

$$306 \quad Q_{lw}^{in} = Q_{lw\_c}^{in}(1 - N^4) + 0.952N^4 \sigma_{sb} T_{ak}^4 \quad (11)$$

307 where  $Q_{lw\_c}^{in}$  is the incoming longwave radiation under the clear sky;  $\varepsilon_{ac}$  is the clear sky atmospheric emissivity calculated  
 308 using Eq. (8) by Satterlund (1979);  $T_{ak}$  is the air temperature in K;  $e_s$  and  $e_a$  are the saturated and actual vapour pressure of  
 309 water, respectively;  $RH$  is the relative humidity;  $T_a$  is the air temperature in degree Celsius;  $N$  is the fractional cloud cover.  
 310 Note that Eq. (11) was developed by Konzelmann et al. (1994).

311

312  $Q_E$  was calculated using the equation suggested by Ryan et al. (1974) following Yang et al. (2023):

$$313 \quad Q_E = \left[ 2.70 \left( \frac{T_{wk}}{1-0.378(e_s/P)} - \frac{T_{ak}}{1-0.378(e_a/P)} \right)^{\frac{1}{3}} + 3.2V \right] (e_s - e_a) \quad (12)$$

314 where  $P$  is the atmospheric pressure;  $V$  is the wind speed.  $Q_H$  was calculated from  $Q_E$  using Bowen's ratio  $B$  as follows:

$$315 \quad B = \frac{C_a P}{0.622 l_v} \times \frac{T_s - T_a}{e_s - e_a} \quad (13)$$

$$316 \quad Q_H = B Q_E \quad (14)$$

317 where  $C_a$  is the specific heat of air;  $l_v$  is the latent heat of vaporization;  $T_s$  is the surface water temperature. In a previous study,  
 318 Yang et al. (2023) investigated various formulas used to calculate incoming longwave radiation and the latent and sensible  
 319 heat fluxes during freeze-up on the North Saskatchewan River in Alberta, and the combination of formulas (Eqs. 7~14) used  
 320 in this study were the ones that provided the most accurate results in Yang et al (2023). It is also worth noting that only hourly  
 321 meteorological data were available for the KR and PR regions as described in Sec. 3. As a result, the heat fluxes were calculated  
 322 on a 1-hour time interval for the KR and PR deployments, and for all the NSR deployments the heat fluxes were calculated on  
 323 a 10-min time interval.

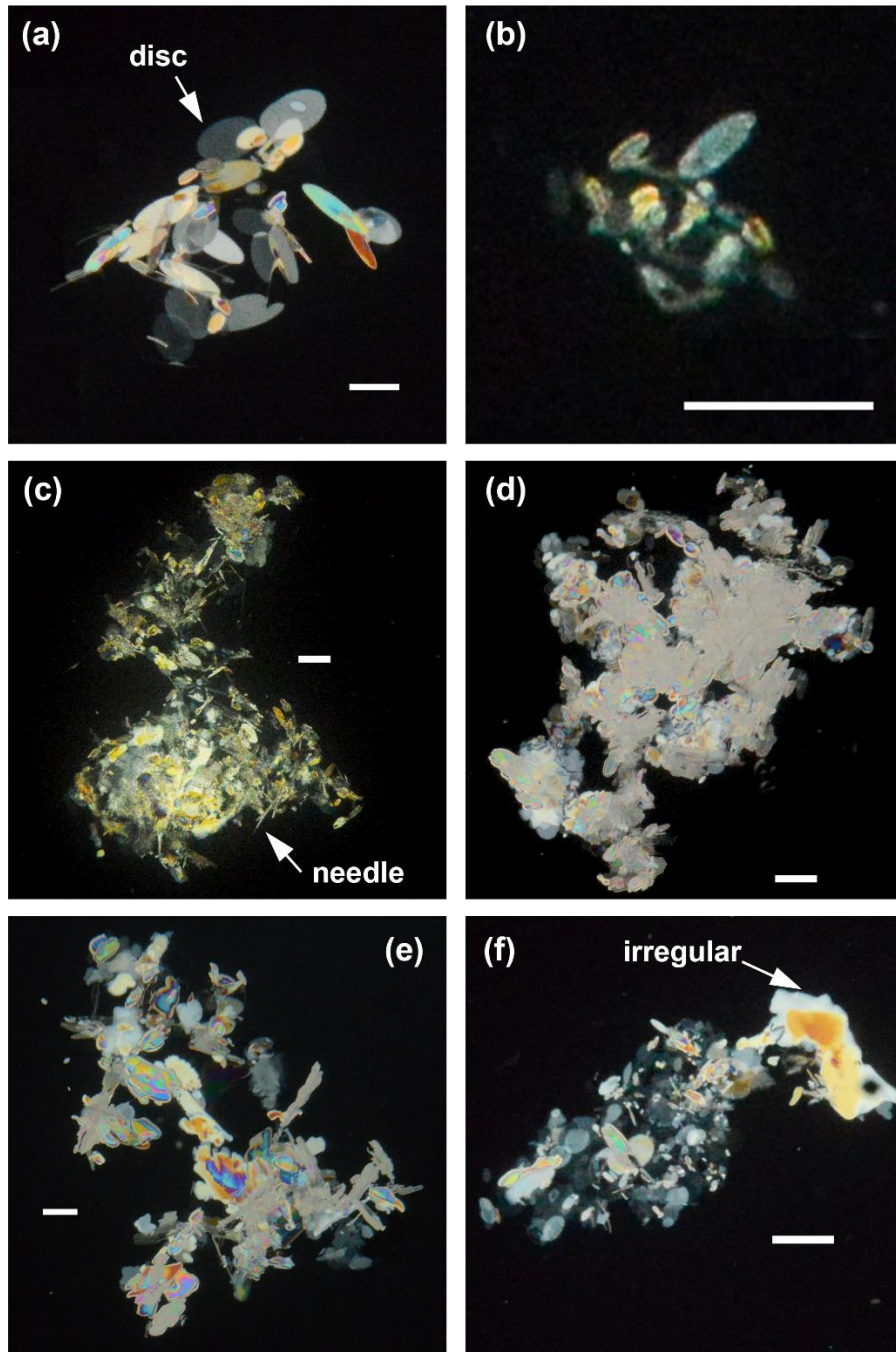
## 324 5 Results

### 325 5.1 Floc shape, size and concentration

326 In Fig. 67 images of typical shapes of frazil flocs observed during the different field deployments are presented. Flocs from  
327 NSR deployments (Figs. 6a7a~b) were comprised predominantly of disc-shaped frazil ice particles of varying sizes  
328 ~~sintered~~frozen together. The floc shown in Fig. 6b7b is representative of flocs observed during deployments NSR-L3 and  
329 NSR-L6. As can be seen, it was comprised of much smaller individual particles than the flocs observed during the rest of the  
330 NSR deployments (Fig. 6a7a). Flocs from deployment PR-F1 (Fig. 6e7c) were comprised of disc-shaped particles, irregular  
331 particles, and some needle-shaped particles. Flocs from deployment KR-E1 (Fig. 6d7d) were formed primarily by densely  
332 aggregated irregular particles and some small disc-shaped particles. Flocs from deployments PR-F2, KR-F1 (Fig. 6e7e), and  
333 KR-F2 (Fig. 6f7f) were mostly comprised of disc-shaped and irregular particles, images of flocs from PR-F2 were not shown  
334 since they are similar to those shown in Figs. 6e7e-f.

335

336 Table 4 presents the number of flocs  $N_T$ , mean size  $\bar{\mu}_f$ , standard deviation  $\sigma_f$ , 95<sup>th</sup> percentile and maximum of the floc size  $S_f$ ,  
337 average floc number concentration  $\bar{C}_{fn}$ , and average volumetric concentration  $\bar{C}_{fv}$  for each deployment. The supercooling  
338 phase, the minimum water temperature  $T_p$ , and average net surface heat flux  $\bar{Q}_n$  are also presented. Deployments NSR-L1,  
339 NSR-L3, and NSR-L4 captured the principal supercooling phase (Principal), while the rest captured only the residual  
340 supercooling phase (Residual).  $T_p$  ranged from -0.021 °C to -0.031 °C for Principal deployments, and from -0.007 °C to -  
341 0.017 °C for Residual deployments. In all deployments  $\bar{Q}_n$  was positive indicating an overall heat loss.  $N_T$  varied significantly  
342 ranging from 442 to 187,288 with the largest  $N_T$  of 187,288 occurring during deployment KR-E1. The mean floc size  $\bar{\mu}_f$   
343 ranged from 1.19 to 5.64 mm with an overall average of 3.8 mm and  $\sigma_f$  ranged from 0.88 to 5.03 mm.  $S_{f95}$  was greater than  
344 ~8 mm except for deployments NSR-L3 and NSR-L6 with values of 4.44 mm and 2.47 mm, respectively. The largest value of  
345  $S_{fmax}$ , 99.69 mm, was observed during KR-E1 which also had the largest number of flocs. The average floc number  
346 concentration  $\bar{C}_{fn}$  varied by three orders of magnitude from  $1.80 \times 10^{-4}$  to  $1.15 \times 10^{-1} \text{ cm}^{-3}$ , and the average floc volumetric  
347 concentration  $\bar{C}_{fv}$  over four orders of magnitude from  $2.05 \times 10^{-7}$  to  $4.56 \times 10^{-3}$ .



348

349 **Figure 67:** Images of frazil flocs of different sizes and shapes from the following deployments: (a) NSR-L1, (b) NSR-L6, (c) PR-F1,  
 350 (d) KR-E1, (e) KR-F1, and (f) KR-F2. The white scale bar in each image represents a length of 3 mm. Note that in some images the  
 351 surrounding ice particles were masked out to highlight the floc at the centre of the image.

352 **Table 4: Supercooling phase, minimum water temperature  $T_p$ , mean net surface heat flux  $\overline{Q_n}$ , number of flocs  $N_T$ , mean floc size**  
353  **$\overline{\mu_f}$ , standard deviation  $\sigma_f$ , 95<sup>th</sup> percentile of floc size  $S_{f95}$ , maximum floc size  $S_{fmax}$ , average floc number concentration  $\overline{C_{fn}}$ , and**  
354 **average volumetric concentration  $\overline{C_{fv}}$  for each deployment.**

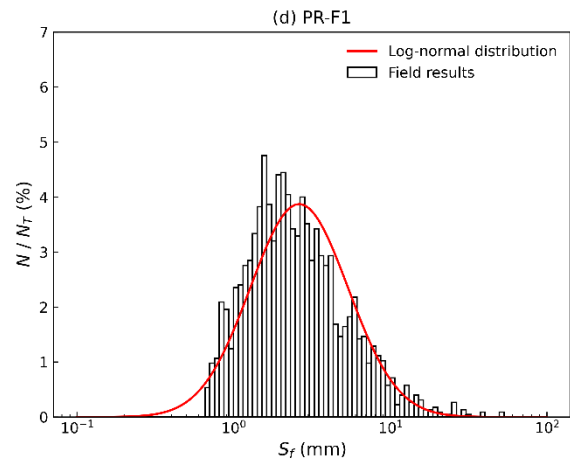
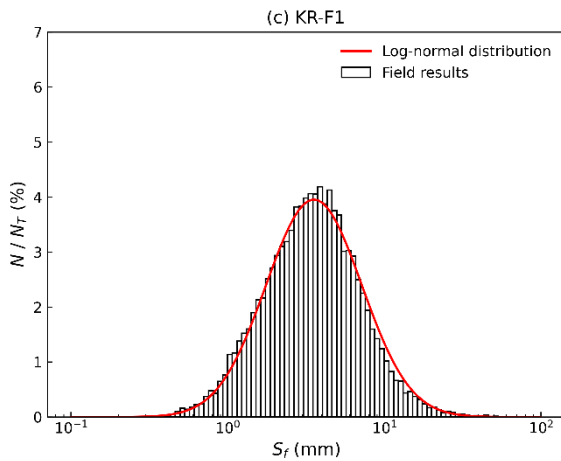
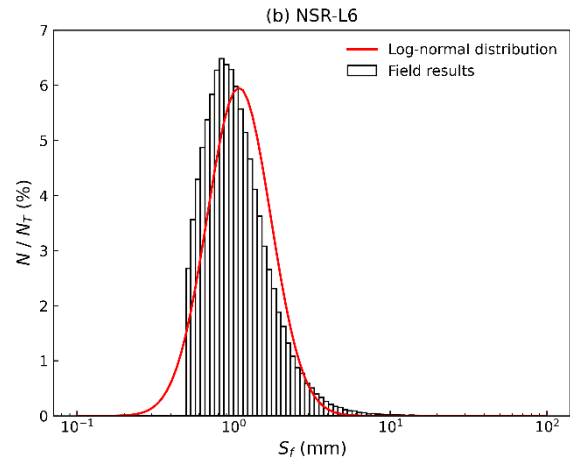
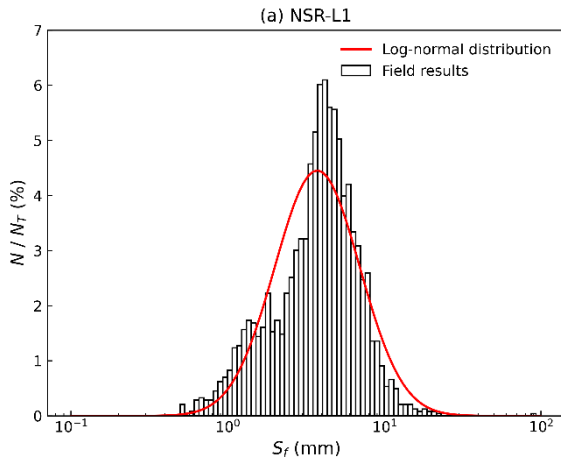
Deployment No.	Supercooling phase	$T_p$ (°C)	$\overline{Q_n}$ (W m <sup>-2</sup> )	$N_T$	$\overline{\mu_f}$ (mm)	$\sigma_f$ (mm)	$S_{f95}$ (mm)	$S_{fmax}$ (mm)	$\overline{C_{fn}}$ (cm <sup>-3</sup> )	$\overline{C_{fv}}$ (cm <sup>3</sup> cm <sup>-3</sup> )
NSR-L1	Principal	-0.021	183.3	2,428	4.33	3.08	8.73	89.58	$9.65 \times 10^{-4}$	$1.39 \times 10^{-5}$
NSR-L2	Residual	-0.009	199.5	879	3.70	2.31	7.54	24.05	$2.72 \times 10^{-4}$	$1.39 \times 10^{-6}$
NSR-L3	Principal	-0.023	95.4	839	1.87	1.31	4.44	9.02	$3.06 \times 10^{-4}$	$2.05 \times 10^{-7}$
NSR-L4	Principal	-0.031	110.3	442	4.50	2.45	8.37	18.53	$1.80 \times 10^{-4}$	$1.21 \times 10^{-6}$
NSR-L5	Residual	-0.016	121.8	631	3.50	2.57	8.40	14.31	$2.60 \times 10^{-4}$	$1.19 \times 10^{-6}$
NSR-L6	Residual	-0.017	157.5	143,097	1.19	0.88	2.47	47.16	$6.75 \times 10^{-2}$	$2.99 \times 10^{-5}$
PR-F1	Residual	-0.009	318.8	2,250	3.43	3.72	9.16	53.35	$1.11 \times 10^{-3}$	$1.84 \times 10^{-5}$
PR-F2	Residual	-0.007	107.4	1,247	4.25	5.03	13.60	53.81	$5.63 \times 10^{-4}$	$1.68 \times 10^{-5}$
KR-E1	Residual	-0.008	243.3	187,288	5.64	4.79	14.28	99.69	$1.15 \times 10^{-1}$	$4.56 \times 10^{-3}$
KR-F1	Residual	-0.010	122.4	23,670	4.43	3.86	10.69	81.38	$1.05 \times 10^{-2}$	$2.32 \times 10^{-4}$
KR-F2	Residual	-0.011	275.2	15,151	4.69	4.08	11.89	68.37	$6.62 \times 10^{-3}$	$1.59 \times 10^{-4}$

355

## 356 5.2 Floc size distribution

357 In Fig. 78, plots of the frazil floc size distribution as well as fitted lognormal distribution curves for four deployments are  
358 presented. All of the size distributions obtained from NSR deployments closely resemble deployment NSR-L1 shown in Fig.  
359 7a8a, except for deployment NSR-L6 shown in Fig. 7b8b. Size distributions from the KR and PR are well represented by  
360 deployments KR-F1 and PR-F1 which are shown in Fig. 7e8c and Fig. 7d8d, respectively. It can be seen from Fig. 78 that a  
361 theoretical lognormal distribution is a reasonable fit to all of the size distributions but a particularly good fit for deployment  
362 KR-F1. This may be attributed to the order-of-magnitude larger sample size for KR-F1 (23,670) compared to NSR-L1 (2,428)  
363 and PR-F1 (2,250). The size distribution for NSR-L6 shown in Fig. 7b8b has the most flocs of the four deployments plotted  
364 with a sample size of 143, 097 but it does not fit a lognormal distribution as closely as the others. This is because the distribution  
365 was cut off at 0.5 mm to eliminate sediment particles. A similar condition can also be observed for PR-F1 shown in Fig. 7d8d  
366 where the cut-off was 0.68 mm. Note that the cut-offs were applied to all size distributions but only impacted the distribution  
367 significantly if there were a significant number of smaller flocs detected.

368



369

370

371 **Figure 78.** Distributions of floc size  $S_f$  for deployments (a) NSR-L1, (b) NSR-L6, (c) KR-F1, and (d) PR-F1. The red line denotes a  
 372 fitted lognormal distribution,  $N$  is the number of flocs in each bin, and  $N_T$  is the total number of flocs.

### 373 5.3 Time series

374 Time series plots of water ~~temperature and air temperatures~~  $T_w$  and  $T_a$ , heat flux  $Q$ , floc mean size  $\mu_f$ , floc number  
 375 concentration  $C_{fn}$ , and floc volumetric concentration  $C_{fv}$  for deployments NSR-L4, KR-F1, and PR-F2 are presented in Figs.  
 376 ~~8, 9 and 10, respectively-9, 10 and 11, respectively~~ (Note that similar time series plots for the other eight deployments are  
 377 presented as Figs. S1-S8 in the Supplement). Deployment NSR-L4 occurred during the principal supercooling phase and is the  
 378 only deployment that captured the entire principal supercooling phase, while KR-F1 and PR-F2 captured the middle and end  
 379 of the residual supercooling phase, respectively.

380

381 During NSR-L4 (Fig. [8a9a](#)) supercooling started at 15:25 and after that  $T_w$  decreased almost linearly at a cooling rate of -  
382  $0.0009\text{ }^\circ\text{C min}^{-1}$ , reached a  $T_p$  of  $-0.031\text{ }^\circ\text{C}$  (i.e., peak supercooling) at 16:02 and then started to increase and reached a stable  
383 residual temperature of  $-0.010\text{ }^\circ\text{C}$  at 16:37. [Figure 8b](#)  $T_a$  decreased from  $-1.7$  to  $-7.2\text{ }^\circ\text{C}$  with an average of  $-4.6\text{ }^\circ\text{C}$ . [Figure 9b](#)  
384 shows that the net heat flux  $Q_n$  increased from  $26\text{ W m}^{-2}$  to  $150\text{ W m}^{-2}$  primarily due to the decrease in the magnitude of  
385 shortwave radiation  $Q_{sw}$ . The rest of the heat flux components remained positive (heat loss) and relatively stable throughout  
386 the deployment, with  $Q_{lw}$  being the dominant component. In Fig. [8e9c](#)  $\mu_f$  began increasing significantly  $\sim 7$  minutes before  
387 the peak supercooling temperature was reached, reaching a maximum of  $7.8\text{ mm}$   $\sim 37$  minutes after peak supercooling, then it  
388 decreased to  $\sim 6\text{ mm}$  and remained approximately constant afterwards. [Figure 8d9d](#) shows that significant numbers of frazil  
389 particles were detected  $\sim 15$  minutes before peak supercooling with  $C_{fn}$  values below  $2 \times 10^{-4}\text{ cm}^{-3}$ . At  $\sim 2$  minutes before peak  
390 supercooling  $C_{fn}$  increased rapidly and peaked  $\sim 30$  minutes after peak supercooling at a value of  $9.3 \times 10^{-4}\text{ cm}^{-3}$  and then  
391 decreased to  $2 \times 10^{-4}\text{ cm}^{-3}$  at the end of the deployment. [Figure 8e9e](#) shows that  $C_{fv}$  only increased notably after peak  
392 supercooling and reached a value of  $8.8 \times 10^{-6}$   $\sim 30$  minutes after the peak supercooling. After that it decreased before spiking  
393 to  $1.6 \times 10^{-5}$   $\sim 38$  minutes after the peak supercooling and then decreased to  $1.7 \times 10^{-6}$  at the end. An examination of the images  
394 showed that the spike was caused by several large flocs up to  $18.5\text{ mm}$  in size.

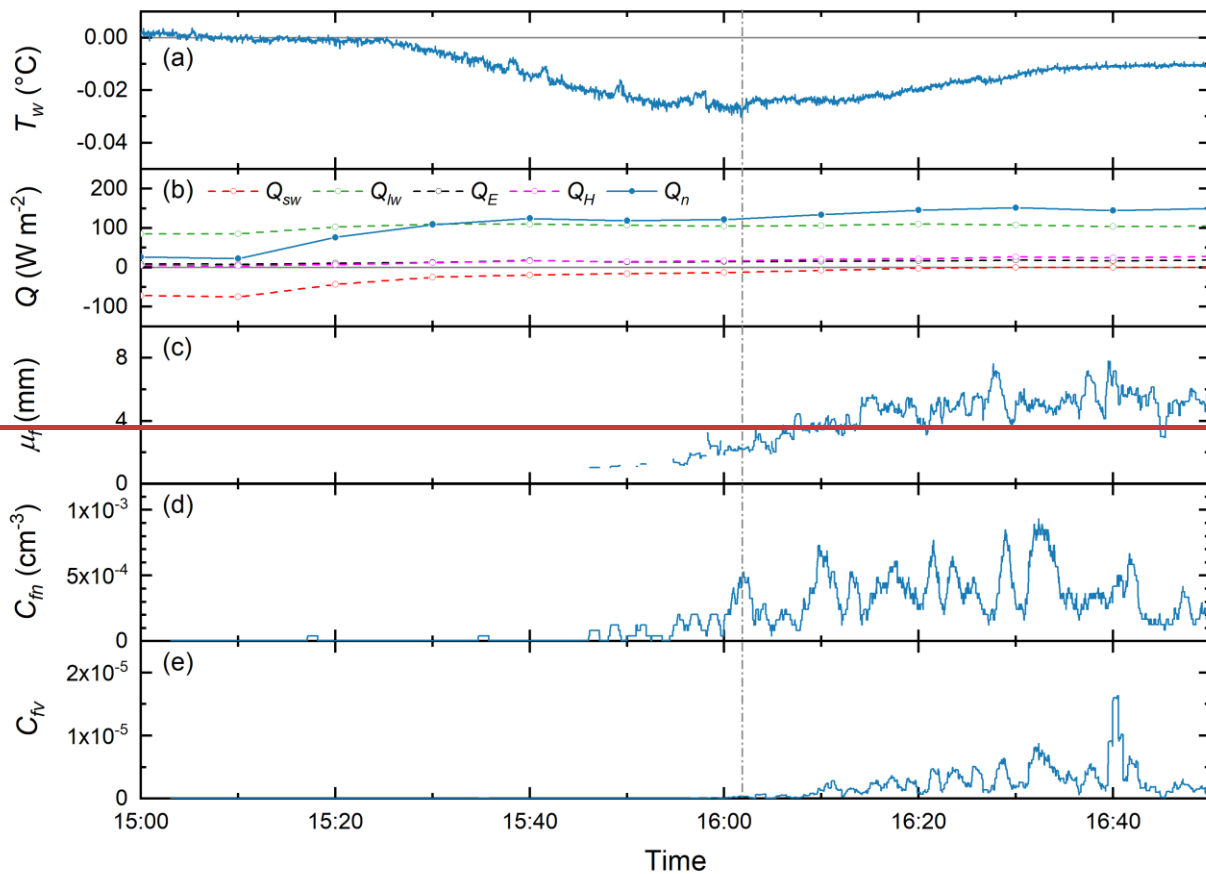
395

396 During KR-F1,  $T_w$  fluctuating continuously around  $-0.008\text{ }^\circ\text{C}$ , except for one anomalous spike that occurred at 17:03 (Fig.  
397 [9a10a](#)), which was caused by ice contacting the sensor when the polarizers were being rinsed. Additionally, periodic upward  
398 spikes with a period of 1 minute and magnitude of  $\sim 0.001\text{ }^\circ\text{C}$  were visible on the plot. While the cause of these spikes remains  
399 uncertain, it is worth noting that their magnitude falls within the range of accuracy of the sensor. [In Fig. 9b](#) The air temperature  
400 was relatively stable with  $T_a$  varying between  $-10$  to  $-12\text{ }^\circ\text{C}$ . [In Fig. 10b](#),  $Q_n$  rose during the deployment from  $-2\text{ W m}^{-2}$  to  $261$   
401  $\text{W m}^{-2}$  largely due to the decrease in the magnitude of  $Q_{sw}$ . Note that the heat flux components here were computed on a 1-  
402 hour time interval. In Figs. [9e10c-e](#), there are gaps in the data during these time periods 15:33  $\sim$  15:38, 16:17  $\sim$  16:23, 16:58  
403  $\sim$  17:04, and 17:34  $\sim$  17:39, that are visible as short time series segments with zero slope. These were created when the images  
404 collected during the time periods when the polarizers were being rinsed were removed from the dataset. In Fig. [9e10c](#),  $\mu_f$   
405 fluctuated around  $\sim 4\text{ mm}$  before significantly increasing at 17:40, eventually reaching  $5.9\text{ mm}$  by the end of the deployment.  
406 Similar trends are evident in Figs. [9d10d-e](#) for  $C_{fn}$  and  $C_{fv}$ , respectively. At 17:41  $C_{fn}$  started to increase significantly and  
407 reached a peak value of  $4.5 \times 10^{-2}\text{ cm}^{-3}$  at 17:53 while  $C_{fv}$  started to increase significantly at 17:50 and eventually peaked at a  
408 value of  $2.8 \times 10^{-3}$ . A hydropeaking wave arrived at the Fortress site at 17:25 increasing the depth by 19% by the end of the  
409 deployment and causing rapid increases in floc size and concentration.

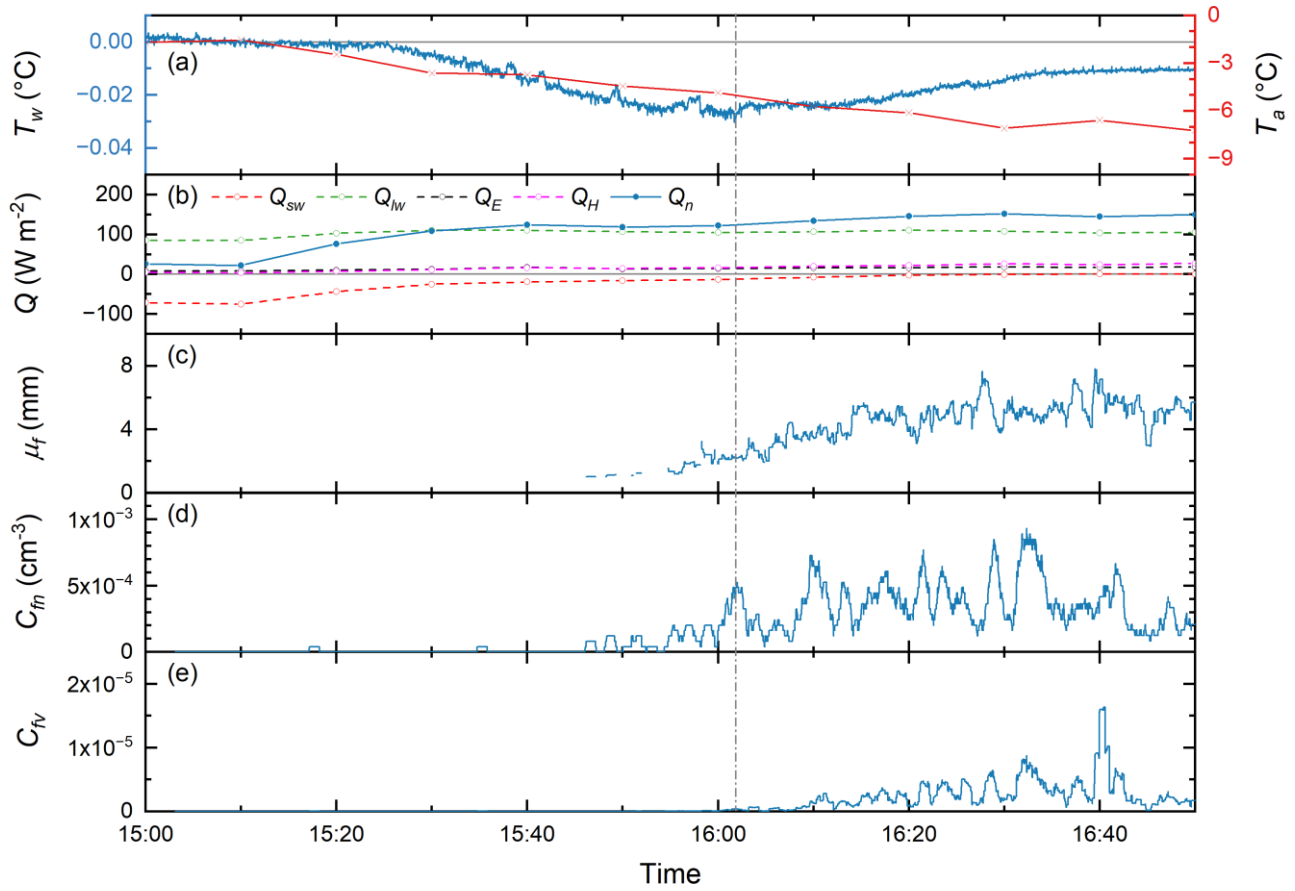
410

411 During deployment PR-F2,  $T_w$  was initially at  $-0.006\text{ }^\circ\text{C}$  but then increased above zero at 10:21, and eventually reached  $0.033$   
412  $^\circ\text{C}$  at the end of the deployment (Fig. [10a](#);[11a](#)). [Figure 10a](#)  $T_a$  followed a similar trend to  $T_w$ , rising from  $-7.6$  to  $-4.1\text{ }^\circ\text{C}$ . The net heat loss  
413  $Q_n$  steadily decreased from  $165\text{ W m}^{-2}$  to  $12\text{ W m}^{-2}$  (Fig. [10b](#);[11b](#)) due to an increase in the magnitude of  $Q_{sw}$ . In Fig. [10e](#);[11c](#)

414  $\mu_f$  fluctuated between 1 mm and 10 mm during the deployment with an average of 4 mm. In Figs. 10d-11d-e the time series of  
 415 number and volume concentrations did not exhibit significant trends.  $C_{fn}$  ranged from  $4.1 \times 10^{-5} \text{ cm}^{-3}$  to  $2.4 \times 10^{-3} \text{ cm}^{-3}$  with  
 416 an average of  $5.6 \times 10^{-4} \text{ cm}^{-3}$  while  $C_{fv}$  was negligible most of the time with occasional spikes up to  $4.2 \times 10^{-4}$ . One spike that  
 417 occurred at 10:39 caused both  $C_{fn}$  and  $C_{fv}$  to reach their peak values. Visual examination of the images shows that at this time  
 418 the number of flocs increased significantly for three consecutive images and this was possibly caused by a large floc colliding  
 419 with the camera frame and fracturing.

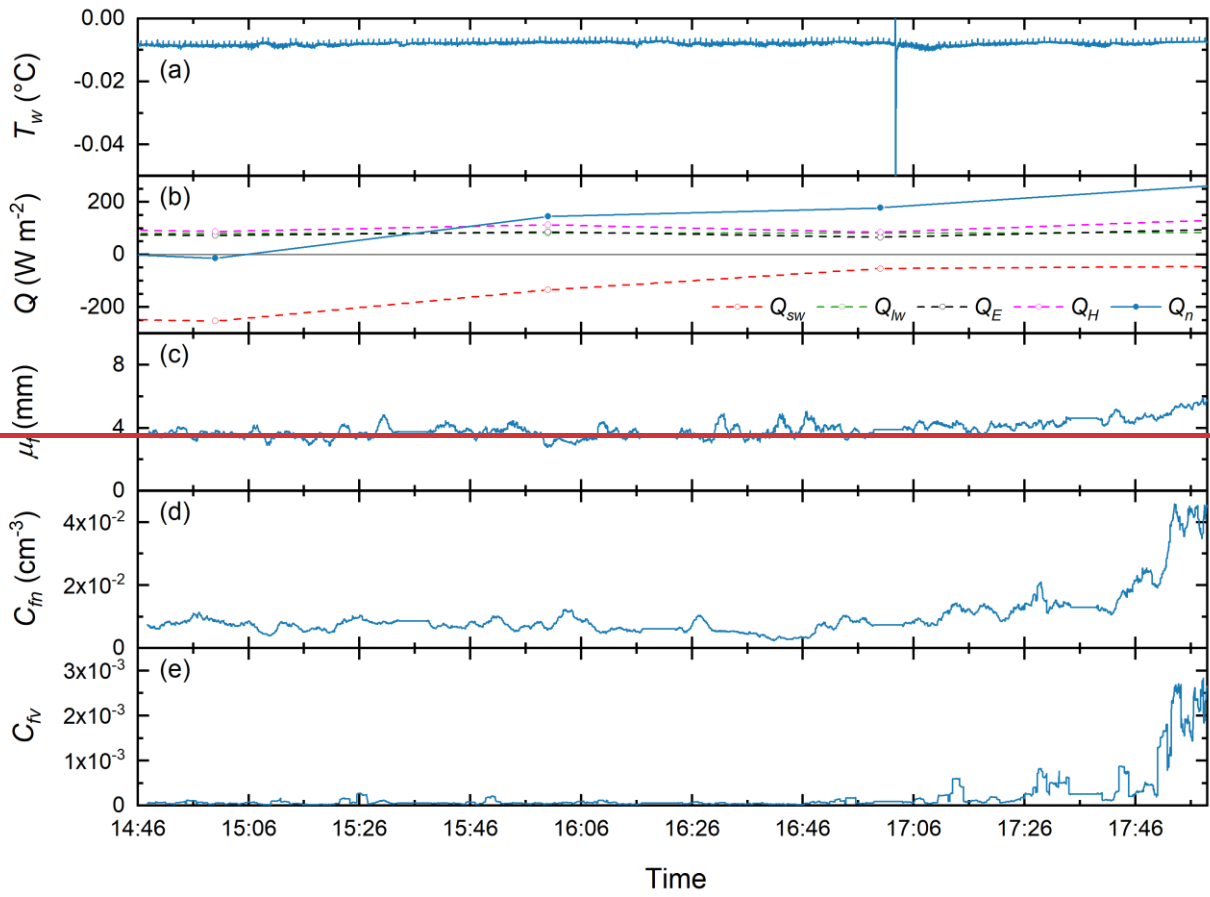


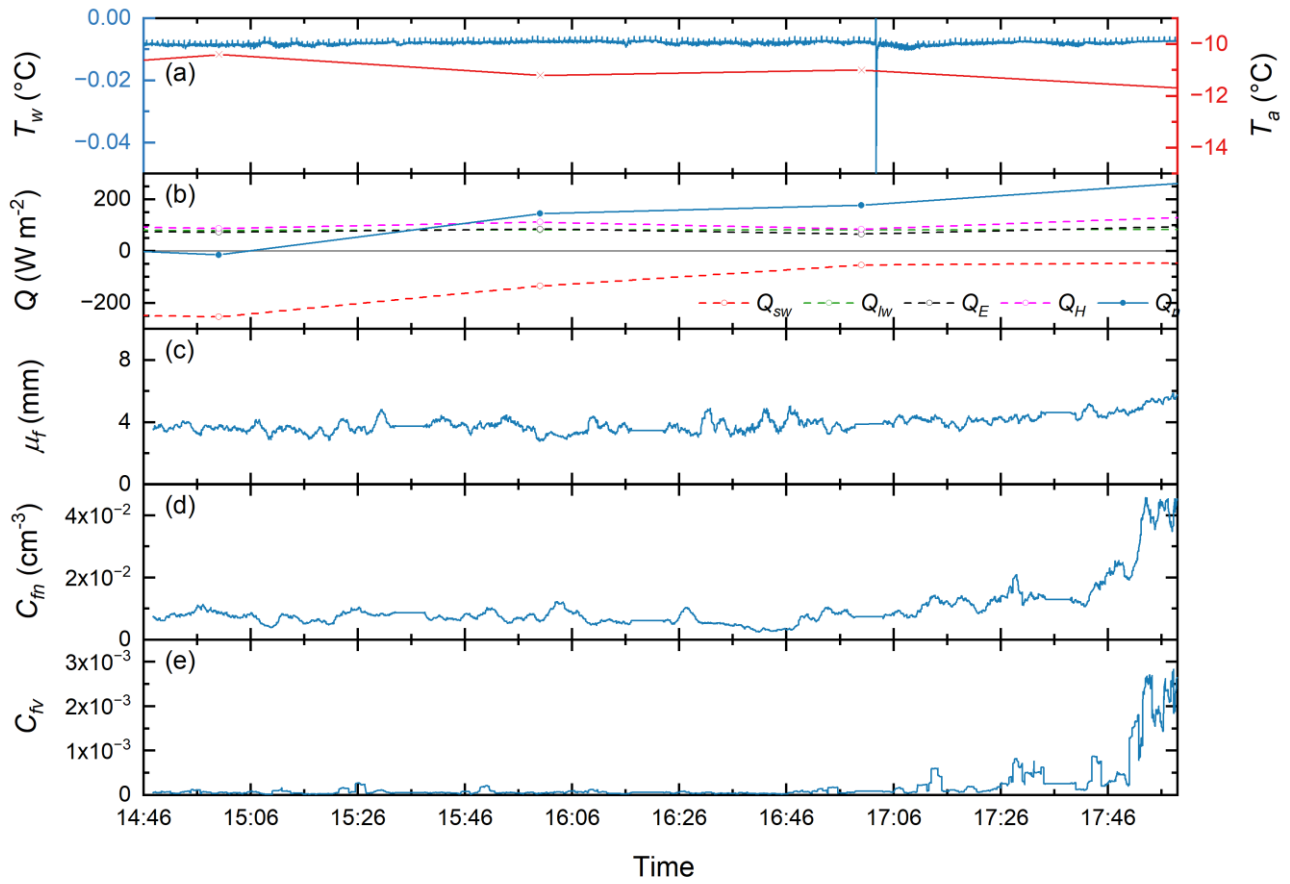
420



421

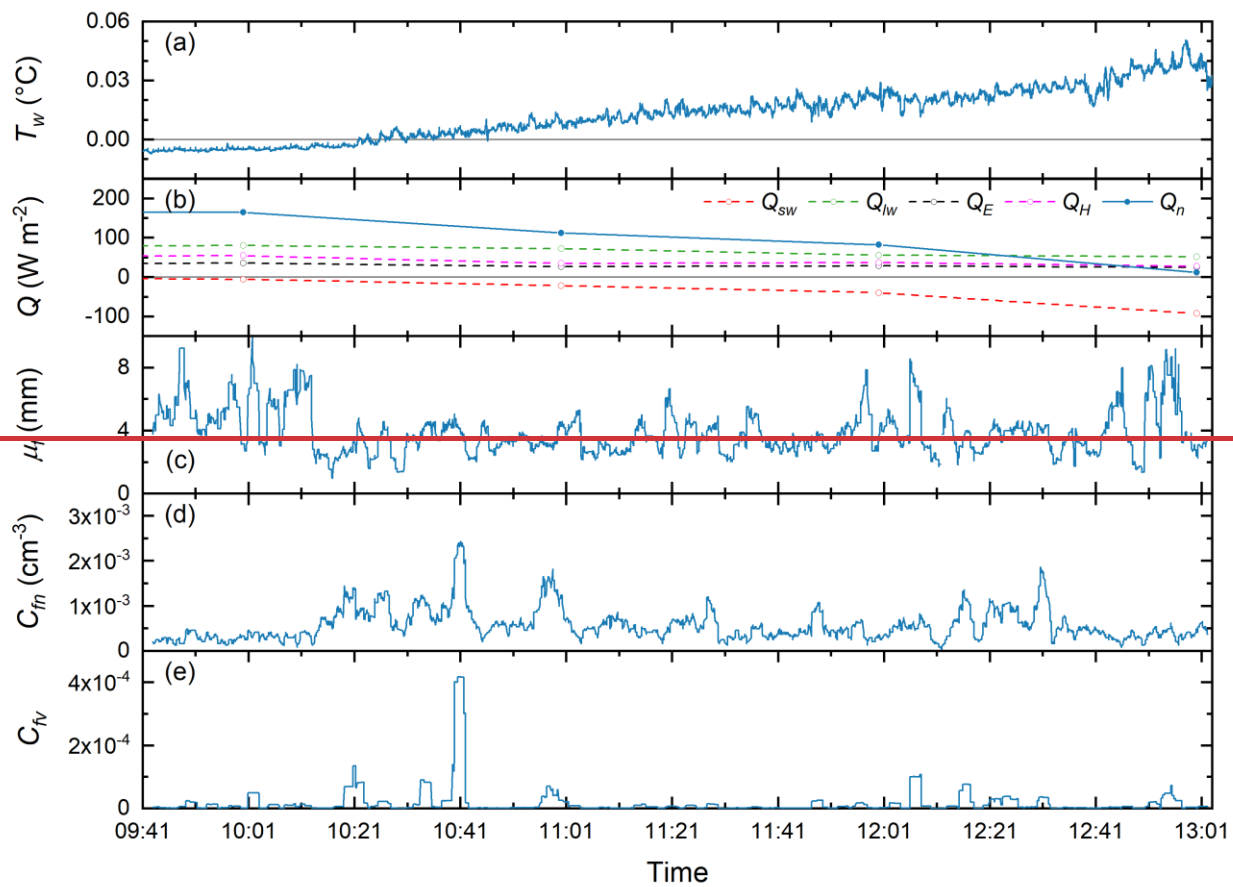
422 **Figure 98.** Time series of (a) water and air temperatures  $T_w$  and  $T_a$ , (b) heat flux  $Q$ , (c) floc mean size  $\mu_f$ , (d) floc number  
 423 concentration  $C_{fn}$  and (e) floc volumetric concentration  $C_{fv}$  for deployment NSR-L4 on December 12, 2021. The vertical dashed  
 424 grey line indicates the time when the peak supercooling temperature is achieved.

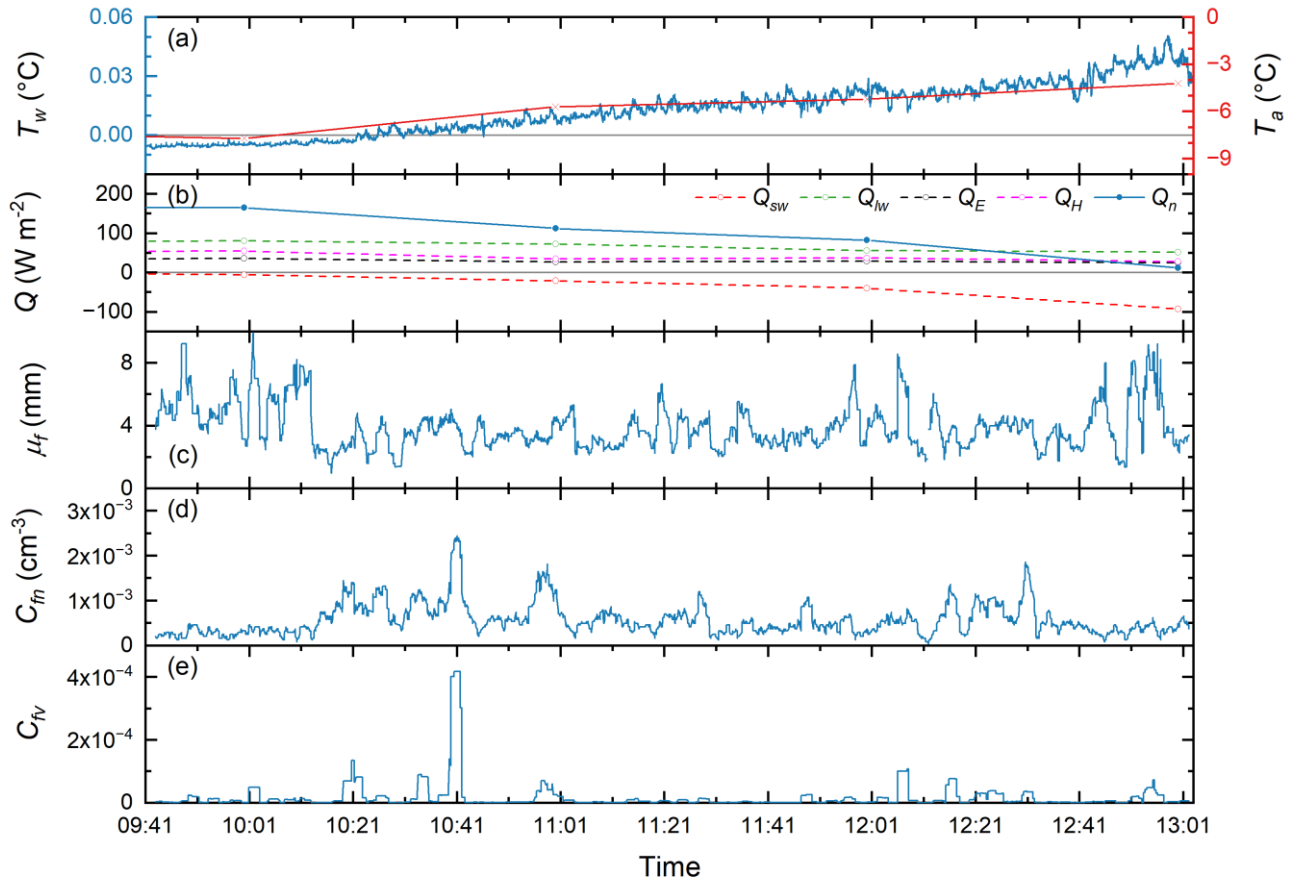




426

427 **Figure 109.** Time series of (a) water and air temperatures  $T_w$  and  $T_a$ , (b) heat flux  $Q$ , (c) floc mean size  $\mu_f$ , (d) floc number  
 428 concentration  $C_{fn}$  and (e) floc volumetric concentration  $C_{fv}$  for deployment KR-F1 on January 30, 2023.





430

431 **Figure 1011.** Time series of (a) water and air temperatures  $T_w$  and  $T_a$ , (b) heat flux  $Q$ , (c) floc mean size  $\mu_f$ , (d) floc number  
 432 concentration  $C_{fn}$  and (e) floc volumetric concentration  $C_{fv}$  for deployment PR-F2 on December 13, 2022.

## 433 6 Discussion

434 Images of typical frazil flocs shown in Fig. 67 illustrate the complexity of their morphology, which encompasses various ice  
 435 crystal shapes, including disc-shaped, needle-shaped, and irregular particles. Disc-shaped ice particles were observed in flocs  
 436 from all three rivers but were most pronounced in the NSR where flocs were almost all formed by disc-shaped particles of  
 437 different sizes (Figs. 6a-b). Flocs containing needle-shaped crystals as shown in Fig. 6e7a-b). The growth of frazil ice in  
 438 supercooled water is limited by the diffusive removal of the latent heat of solidification from the ice-water interface and by  
 439 the slow attachment kinetics in the perpendicular direction, which leads to the formation of disc-shaped particles (Mullins and  
 440 Serkerka, 1964; Rees Jones and Wells, 2015). Flocs containing needle-shaped crystals as shown in Fig. 7c were observed  
 441 during deployment PR-F1 which had a very low mean air temperature of -20.64 °C. These types of crystals have been found  
 442 to form primarily at the surface of supercooled water (Hallett, 1959; Clark and Doering, 2002). The cold air temperature during

443 deployment PR-F1 may have promoted the growth of these needle-shaped particles at the water surface before they were  
444 entrained in the water column and subsequently attached to flocs. Irregular particles were observed in flocs from both the KR  
445 and PR, most pronouncedly in deployment KR-E1 as shown in Fig. [7d](#). ~~Arakawa (1954) discovered that after reaching a~~  
446 ~~certain size, disc-shaped particles did not maintain their shape in supercooled water and started to grow irregularly around the~~  
447 ~~edge. Therefore, the flocs observed in the PR and KR may have been relatively old, meaning that they had been immersed in~~  
448 ~~supercooled water for a sufficiently long time that they grew irregularly. Conversely, the younger flocs observed in the NSR~~  
449 ~~likely did not have time to grow irregularly. Irregularly shaped particles are formed by unstable disk growth which is known~~  
450 ~~to be caused by the formation of temperature gradients in the water surrounding the particles (Kallungal and Barduhn, 1977).~~  
451 ~~This suggests that during the KR and PR deployments, frazil ice particles probably spent some time in relatively quiescent~~  
452 ~~water where the turbulence intensity was so low that temperature gradients could form in the water surrounding the particles.~~  
453 ~~Another possibility is that the particles were temporarily transported to the river surface exposing them to cold air, which may~~  
454 ~~also lead to unstable disk growth.~~ In addition, broken fragments of skim ice or border ice that were entrained into the water  
455 column are another possible source of irregular particles in flocs. Clark and Doering (2009) observed in the laboratory that  
456 flocs could become denser over time when the turbulence intensity was higher. During deployment KR-E1, although the locally  
457 measured depth-averaged velocity near the FrazilCam was relatively low at  $0.22 \text{ m s}^{-1}$ , the water velocity  $\sim 70 \text{ m}$  upstream of  
458 the deployment site was visually observed to be very turbulent due to the presence of four groins and a narrow channel width.  
459 Therefore, this may have contributed to the denser flocs that were observed during this deployment.

460

461 The data presented in Table 4 and Fig. [78](#) are the first quantitative measurements of frazil floc sizes and concentrations in  
462 rivers. The mean floc size averaged over all deployments was 3.80 mm, which was close to the mean values observed for most  
463 of the individual deployments except for deployments NSR-L3, NSR-L6, and KR-E1 which had mean floc sizes of 1.87, 1.19,  
464 and 5.64 mm, respectively. As noted in Sec. 5.1, flocs observed during deployments NSR-L3 and NSR-L6 were comprised of  
465 much smaller disc-shaped individual particles (Fig. [6b7b](#)) than the rest of the deployments (Fig. [6a7a](#)). Deployment NSR-L3  
466 took place during a principal supercooling event in which the observed small frazil ice particles were likely newly formed and  
467 still growing, which could be the reason why the flocs were smaller and comprised of significantly smaller particles. In  
468 addition, deployment NSR-L3 took place as the crest of a hydropeaking wave was passing the site that resulted in a mean  
469 water depth of 1.24 m which is 37% to 55% larger than the depths during the other NSR deployments (Table 3). The  
470 significantly higher water depth reduced the ~~relative depth~~fractional height where the images were collected, which could also  
471 result in smaller floc sizes. This would be consistent with measurements by Reimnitz et al. (1993) that showed that larger flocs  
472 have higher rise velocities. Deployment NSR-L6 occurred during the 2022 freeze-up season, which was the shortest freeze-up  
473 in  $\sim 10$  years lasting only three days. Significantly smaller flocs were observed during this deployment (see Fig. [6b7b](#)) and this  
474 may be because smaller relatively young flocs were generated during this rapid freeze-up process. The largest mean floc size,  
475 maximum floc size and largest concentration (see Table 4) were observed during deployment KR-E1 (Fig. [6d7d](#)). As discussed  
476 previously the ~~flocs may~~particles that formed flocs during KR-E1 included irregularly shaped particles and this could have

477 ~~been relatively 'older' and therefore resulted in larger flocs compared to newly formed flocs since they experienced longer time~~  
478 ~~periods for both in situ crystal growth and particle accretion. flocs formed entirely by disc-shaped particles.~~

479

480 The mean floc size and standard deviation ranged from 1.19 to 5.64 mm, and 0.88 to 5.03 mm, respectively as shown in Table  
481 4. The 95<sup>th</sup> percentile of floc size ranged from 2.47 to 14.28 mm, and the largest flocs found was 99.69 mm in size. Schneck  
482 et al. (2019) conducted laboratory experiments in a frazil ice tank ~~and with an average turbulent dissipation rate of  $0.034 \text{ m}^2 \text{ s}^{-3}$~~   
483 ~~<sup>3</sup> which falls within the range of the values estimated in the three rivers in this study ( $0.005 \sim 0.207 \text{ m}^2 \text{ s}^{-3}$ ).~~ They found that in  
484 freshwater the size distribution of flocs followed a lognormal distribution and ~~the~~the mean size, 95<sup>th</sup> percentile of floc size,  
485 and maximum size were 2.57 mm, 6.91 mm, and 95.1 mm, respectively. The mean and 95<sup>th</sup> percentile sizes fall within the  
486 range of the values observed in this study ~~and the two maximums are comparable. The. However, the~~ overall mean floc size  
487 observed in the field was 3.80 mm, which is 48% larger than the mean measured in the laboratory. ~~The size distributions~~  
488 ~~obtained from different rivers can all be reasonably fitted with lognormal distribution as shown in Fig. 7, which is consistent~~  
489 ~~with the laboratory measurements (Schneck et al., 2019).~~The maximum floc sizes observed in the laboratory and field are  
490 comparable. It is worth noting that the largest floc size of 99.69 mm was just slightly smaller than the FOV dimensions and  
491 considerably larger than the 3.6 cm gap, indicating that the floc size measurements may have been physically limited by the  
492 FOV and the gap between the polarizers. Therefore, further increases in both the FOV and the gap between the polarizers may  
493 be needed in future studies to allow even larger flocs to be imaged and measured.

494

495 ~~The size distributions obtained from different rivers are all a reasonable visual fit to a lognormal distribution as shown in Fig.~~  
496 ~~8, which is consistent with the laboratory measurements (Schneck et al., 2019). However, when the Chi-square test for~~  
497 ~~goodness-of-fit was applied none of the size distributions were quantitatively confirmed to fit a lognormal distribution at the~~  
498 ~~5% significance level. This could be primarily due to the use of the cut-off size to eliminate sediment particles which produced~~  
499 ~~a sharp cut-off in the distributions. In addition, the small number of samples in some deployments resulted in noisy size~~  
500 ~~distributions making it unlikely that they would be a good quantitative fit to a smooth lognormal distribution. Nonetheless, the~~  
501 ~~good qualitative comparison of the floc size distributions measured in the field with theoretical lognormal distributions in Fig.~~  
502 ~~8 does suggest that if the sample size was larger and sediment particles could be filtered out that floc size distributions in rivers~~  
503 ~~would also closely follow a lognormal distribution.~~

504

505 The average floc number concentration  $\overline{C_{fn}}$  ranged from  $1.80 \times 10^{-4}$  to  $1.15 \times 10^{-1} \text{ cm}^{-3}$  (Table 4), Schneck et al. (2019)  
506 measured a peak floc number concentration of  $2.5 \times 10^{-1} \text{ cm}^{-3}$  in freshwater laboratory experiments, which is similar in  
507 magnitude to the upper limit of values measured in the field. The average floc volumetric concentration  $\overline{C_{fv}}$  ranged from  $2.05$   
508  $\times 10^{-7}$  to  $4.56 \times 10^{-3}$  (Table 4). Previous studies reported suspended ice volumetric concentrations ranged from  $2 \times 10^{-6}$  to  $6 \times$   
509  $10^{-3}$  (Tsang, 1984; Marko and Jasek, 2010; Richard et al., 2011). These measurements were made using comparative resistance  
510 probes and acoustic devices which in theory detect all of the ice suspended in the water. The upper range of previous

511 concentration measurements is comparable to that reported in this study. However, the lower range is one order of magnitude  
512 larger than this study, which may be due to the fact that the previous studies reported the total volume of frazil flocs and  
513 particles.

514

515 The time series of frazil floc properties in Fig. 89 indicate that during the principal supercooling phase, floc number and mean  
516 size started to increase significantly just prior to peak supercooling and reached a maximum near the end of principal  
517 supercooling, the floc volumetric concentration only started to increase significantly after peak supercooling occurred.  
518 Deployment NSR-L3 that ~~also~~ captured almost the entire principal supercooling phase also showed a similar trend- (see Fig.  
519 S3 in the Supplement). The increasing trend of floc mean size and number concentration generally agrees with previous  
520 laboratory measurements (Schneck et al., 2019; Pei et al., 2023). However, laboratory measured mean floc size and number  
521 concentration stopped increasing significantly shortly after peak supercooling, while in the field they stopped increasing later,  
522 near the end of the principal supercooling period. For example, Schneck et al. (2019) observed that the mean floc size and  
523 number concentration in freshwater stopped increasing significantly at dimensionless times of  $t / t_c = 1.13$  and  $1.27$ ,  
524 respectively compared to  $t / t_c = 2.00$  and  $1.81$  for NSR-L4 ( $t_c$  is the time interval between the start of supercooling and peak  
525 supercooling and  $t$  is the time). The peak floc number concentration measured during the three Principal deployments in this  
526 study ranged from  $9.3 \times 10^{-4} \text{ cm}^{-3}$  to  $3.1 \times 10^{-3} \text{ cm}^{-3}$ , which was more than two orders of magnitude lower than the  $2.5 \times 10^{-1}$   
527  $\text{cm}^{-3}$  measured in the laboratory tank by Schneck et al. (2019). These significantly lower floc concentrations suggest that  
528 particle concentrations in the field were also much lower compared to laboratory measurements. At lower suspended frazil  
529 concentrations the collision frequency of frazil particles would be reduced, increasing the time for flocs to grow gain mass via  
530 collision-induced particle-floc aggregation, which might explain the longer time period that mean floc size and number  
531 concentration was observed to increase in the field.

532

533 Figure 910 shows that during KR-F1 the mean floc size was approximately constant prior to the arrival of the hydropeaking  
534 wave during the residual supercooling phase. Similarly, there were no trends observed in floc size in five other Residual  
535 deployments, NSR-L2, NSR-L5, KR-E1, PR-F1 (see Figs. S2, S4, S7 and S6 in the Supplement) and PR-F2- (Fig. 11).  
536 McFarlane et al. (2019b) found that in rivers the mean particle size remained approximately constant during the residual  
537 supercooling phase if the environmental conditions were relatively stable. Therefore, it follows that flocs observed during the  
538 residual supercooling phase would also have a stable mean size unless hydraulic and/or meteorological conditions changed  
539 significantly. The mean floc size is the most stable during deployment KR-E1 (Fig. S7 in the Supplement) with a fluctuation  
540 range of only 1.5 mm, which could be in part due to the significantly larger sample size of 187,288. The only two Residual  
541 deployments that did not have a stable mean floc size were NSR-L6 and KR-F2- (Figs. S5 and S8 in the Supplement), and in  
542 both cases, the size decreased and this coincided with minor increases in  $T_w$  ( $\sim 0.005$  °C). These results indicate that during the  
543 residual phase the mean floc size does not typically vary significantly even at the end of the supercooling event when  $T_w$  rises  
544 above zero, as was the case in PR-F1 and PR-F2. During the two PR deployments the floc properties did not change

545 significantly during the 1.3- and 2.5-hour time periods between when supercooling ended, and the measurements stopped. This  
546 is likely because the zero degree isotherm had moved upstream of the deployment site but the frazil being generated upstream  
547 of it was still advecting past the FrazilCam (i.e., the zero degree isotherm was not so far upstream that the advecting frazil had  
548 time to melt.)

549

550 As shown in Fig. 10, during KR-F1 the residual supercooling water temperature remained mostly approximately constant at a  
551 temperature of approximately -0.01°C. An approximately constant residual supercooling temperature was also observed in  
552 NSR-L2, KR-E1 and NSR-L5 (see Figs. S2, S7, and S4 in the Supplement). This means that during the residual supercooling  
553 phase ice was still growing and releasing latent heat that balanced the heat loss from the water surface in order to maintain the  
554 approximately constant water temperature. In this study, although the mean floc size did not vary significantly during most of  
555 the measured residual supercooling deployments, fluctuations and trends in the floc number and volume concentration time  
556 series were observed. This indicates that there may have been frazil ice particles still forming and growing, releasing latent  
557 heat to help balance the surface heat loss. In addition, during the residual phase anchor ice, border ice, and surface ice pans  
558 were likely growing as well and releasing latent heat, helping to maintain the stable residual supercooling temperature.

559

560 The time series of water temperature  $T_w$  and net heat flux  $Q_n$  provided an opportunity to theoretically estimate the total ice  
561 growth in the water column, which could be compared to the measured floc volumetric concentration  $C_{fv}$  to estimate the  
562 fraction of ice sampled by the FrazilCam. Assuming there were no significant water temperature gradients in any direction  
563 (i.e. the river had a uniform temperature) and that the water depth was constant, the thermal balance of the water-ice mixture  
564 is given by:

565 
$$\rho C_p \frac{dT_w}{dt} = -\frac{Q_n}{\bar{d}} + \rho_i L_i \frac{dC_i}{dt}, \quad (15)$$

566 where  $\rho$  is the water density,  $C_p$  is the specific heat of water,  $\rho_i$  is the ice density,  $L_i$  is the latent heat of fusion of ice, and  $C_i$   
567 is the total ice concentration due to thermal growth (Souillé et al., 2023). Eq. (15) was then used to estimate,  $C_i$  for deployment  
568 NSR-L4, which captured the entire principal supercooling period. The result showed that the FrazilCam was only sampling at  
569 most 2% of the total ice that was forming in the water. It should be noted that  $Q_n$  used in the calculation does not account for  
570 the effect of surface ice due to a lack of accurate surface ice data. In addition, mean water depth  $\bar{d}$  was used while in reality  
571 water depth varied spatially and temporally. These approximations create considerable uncertainty in the calculations of the  
572 total heat loss from the surface, and the volume of the water being cooled. Given all the simplifying assumptions that were  
573 made the uncertainty in the calculated  $C_i$  is potentially quite large, but is likely not greater than a factor of two or three.  
574 Therefore, despite this potential large uncertainty, the calculations suggest that the FrazilCam was only sampling less than  
575 ~5% of the total ice being formed in the river. Similar calculations were also performed using data collected in a laboratory  
576 frazil ice tank experiment using the laboratory version of the FrazilCam. In the laboratory environment the water depth is a

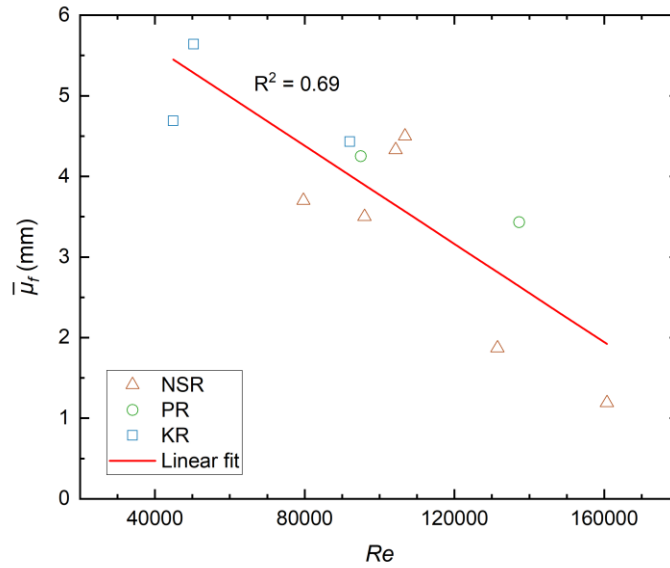
577 constant, the tank has been shown to be well mixed and the surface heat loss can be quantified from the water cooling rate  
578 with reasonable accuracy. These results showed that  $C_i$  calculated using Eq. (15) was comparable to the volumetric  
579 concentration of suspended ice calculated from the FrazilCam images prior to when flocs began rising to the surface. This  
580 demonstrates that the FrazilCam does provide accurate measurements of the suspended ice concentrations. However, the only  
581 time the FrazilCam would be sampling a significant fraction of the total ice being formed in a river would be when suspended  
582 frazil is the only ice that is actively growing.  
583

584 The effect of surface heat flux on floc properties was investigated. A positive mean net heat flux  $\overline{Q_n}$  was observed for all  
585 deployments indicating a net heat loss from the surface. The magnitude of  $\overline{Q_n}$  ranged from 95.4 to 318.8 W m<sup>-2</sup> as shown in  
586 Table 4. The dominant positive heat flux was  $Q_{lw}$  and  $Q_H$  for six and five deployments, respectively, while the dominant  
587 negative heat flux in all deployments was  $Q_{sw}$  which is consistent with previous studies (McFarlane and Clark, 2021; Boyd et  
588 al., 2023). Efforts were made to correlate the mean net heat flux  $\overline{Q_n}$  with the measured floc properties listed in Table 4 (i.e.,  
589 columns 5~11) ~~but no~~. No significant correlations were found when using data from all deployments or when only the data  
590 from the six NSR deployments that have 10-min heat flux data were used. It is worth noting that the heat flux analysis in this  
591 study did not account for varying surface ice concentrations and neglected several heat fluxes (e.g. sediment-water).  
592 ~~Therefore~~ Clearly, more comprehensive and frequent measurements of heat fluxes and surface ice properties are needed in  
593 future studies to more fully understand the impact of varying heat fluxes on frazil floc properties.

594  
595 To investigate the effect of hydraulic conditions on the mean floc size  $\mu_f$ , the local Reynolds number  $Re$  is plotted versus  $\overline{\mu_f}$   
596 in Fig. ~~4+12~~ along with the following linear regression equation:

$$597 \overline{\mu_f} = 6.82 - 3.05 \times 10^{-5} Re, \quad (716)$$

598 As  $Re$  increases from ~40,000 to ~160,000,  $\overline{\mu_f}$  decreases from approximately 5.5 mm to 2 mm and the coefficient of  
599 determination ( $R^2$ ) is 0.69, indicating that the two are moderately correlated. Clark and Doering (2009) found that higher  
600 turbulence intensity inhibited the formation of large flocs. This finding is consistent with the correlation presented in Fig. ~~4+12~~  
601 if it is assumed that turbulence intensity increased with  $Re$  in the three study rivers. However, this is not necessarily the case.  
602 An alternate explanation for the observed correlation is that as  $Re$  increased flocs experienced higher shear strain rates (i.e.,  
603 larger velocity gradients) and more violent floc-floc collisions which would tend to rupture larger flocs and reduce their mean  
604 size.

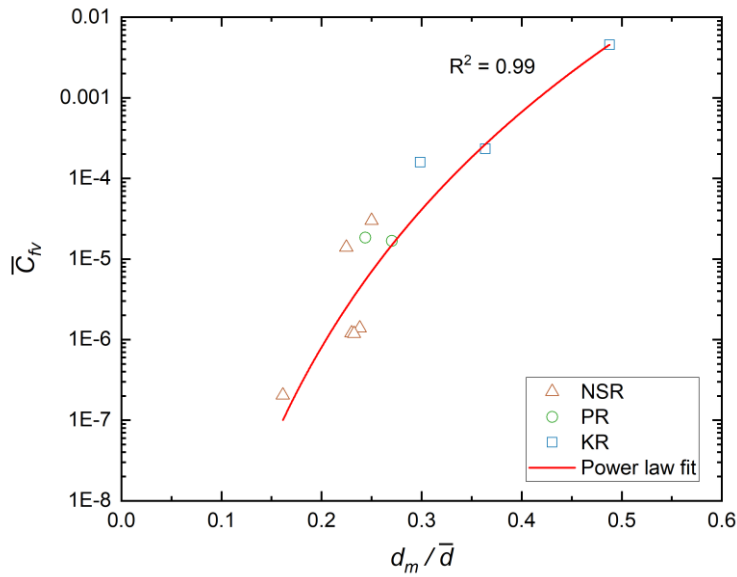


605  
 606 **Figure 412. Relationship between local Reynolds number  $Re$  and mean floc size  $\bar{\mu}_f$  in mm.**

607  
 608 The effect of water depth on the floc volumetric concentration was investigated by correlating the average volumetric  
 609 concentration with the relative depth fractional height  $d_m/\bar{d}$  where  $d_m = 0.198\text{ m}$  is the depth height above the bed at the  
 610 centre of FrazilCam FOV and  $\bar{d}$  is the mean water depth. Figure 4213 presents a scatter plot of the relative depth fractional  
 611 height  $d_m/\bar{d}$  versus the average floc volumetric concentration  $\bar{C}_{fv}$ . Results show that there is a strong nonlinear correlation  
 612 given by the following power law equation:

613 
$$\bar{C}_{fv} = 4.80 \left( \frac{d_m}{\bar{d}} \right)^{9.69}, \quad (817)$$

614 where the  $R^2$  value equals 0.99. Ye (2002) and Morse and Richard (2009) reported measurements of vertical frazil  
 615 concentration profiles and found that the Rouse equation (Rouse, 1937), previously used to characterize suspended sediment  
 616 concentration profiles, could be used to describe the frazil ice concentration profile. Equation (817) is similar in format to the  
 617 Rouse equation, indicating that the vertical concentration of both frazil particles and flocs may be accurately described by  
 618 power law equations.



619

620 **Figure 1213.** Relationship between the **relative depth fractional height**  $d_m / \bar{d}$  and the average floc volumetric concentration  $\bar{C}_{fv}$

## 621 7 Conclusions

622 A submersible high-resolution camera system was deployed during supercooling in three rivers from 2021 ~ 2023. Images  
 623 from the eleven deployments were analyzed to investigate frazil floc properties and their evolution. Images showed that frazil  
 624 flocs observed in the North Saskatchewan River were predominately formed by disc-shaped particles, while flocs in the Peace  
 625 River and Kananaskis River were comprised of various ice crystal shapes, including disc-shaped, needle-shaped, and irregular  
 626 particles. A lognormal distribution is a reasonable description of floc size distributions in rivers. The mean floc size ranged  
 627 from 1.19 to 5.64 mm and the overall mean floc size was 3.80 mm. The mean floc size in rivers was found to 48% larger than  
 628 was previously observed in the laboratory by Schneck et al. (2019) while the maximum floc size was comparable in the  
 629 laboratory and field. The average floc number concentration ranged from  $1.80 \times 10^{-4}$  to  $1.15 \times 10^{-1} \text{ cm}^{-3}$  and previous laboratory  
 630 measurements fall within the range of the values observed in this study. The estimated average floc volumetric concentration  
 631 ranged from  $2.05 \times 10^{-7}$  to  $4.56 \times 10^{-3}$ , with the upper bound being comparable to previous total ice volume concentration  
 632 measurements while the lower bound is an order of magnitude smaller.

633

634 Time series analysis indicated that during the principal supercooling phase, floc number concentration and mean size increased  
 635 significantly just before peak supercooling and reached a maximum near the end of principal supercooling. This increasing  
 636 trend was also observed in previous laboratory measurements (Schneck et al., 2019; Pei et al., 2023) but the duration of the

637 increasing trend was longer in the field. During the residual supercooling phase, the mean floc size did not typically vary  
638 significantly even 2.5 hours after the water temperature rises above zero degrees. The effect of the air-water heat flux on floc  
639 properties was investigated by conducting a linear regression analysis. However, no significant correlations were found, and  
640 this may be due to the limited dataset or the complexity of the field environment where heat fluxes can vary temporally and  
641 spatially. Future field measurements of floc properties, especially made during the principal supercooling phase and made  
642 continuously along multiple sites along a study reach, are needed to more fully understand the factors that govern their size  
643 and concentration.

644

645 Analysis of the influence of local hydraulic conditions on frazil floc properties showed that as the local Reynolds number  
646 increases, the mean floc size decreases linearly. The resulting equation can be used to estimate mean floc sizes in rivers using  
647 estimates of the mean velocity and depth. It was also shown that the averaged floc volumetric concentration can be related to  
648 the ~~relative depth~~fractional height above the bed through a power law equation. This relationship may be useful for describing  
649 the vertical concentration profiles of frazil flocs.

650

651 The detailed measurements of frazil floc properties and their evolution in rivers ~~reported~~presented in this study could be used  
652 in several ways to enhance numerical modelling of river ice processes- in order to improve predictions of river freeze-up. At  
653 the present time the frazil rise velocity is treated as a calibration parameter in comprehensive river ice process models (e.g.  
654 Shen, 2010; Blackburn and She, 2019). However, it could now be directly estimated by first using Eq. (716) to predict the  
655 mean floc size using the local Reynolds number and then the rise velocity could be predicted using Reimnitz et al. (1993)  
656 measurements. In addition, the reported lognormal size distributions of flocs, as well as time series evolution of mean floc size  
657 and concentrations, measured in rivers for the first time, could provide opportunities ~~for the aforementioned models~~ to  
658 ~~include~~incorporate floc dynamics into numerical models with the goal of improving how realistically ~~these river ice process~~  
659 ~~models~~they simulate frazil ice evolution and surface ice progression.

660

661 In the future, it would be of interest to deploy the FrazilCam in lakes and oceans, where the flow regime and salinity may be  
662 considerably different, to investigate frazil particle and floc properties in these different environments. The FrazilCam system  
663 in principle can be deployed in any sufficiently transparent waters, however, the system would need to be modified to automate  
664 the polarizer rinsing process. This would be challenging but might be possible using a mechanical wiper which would allow  
665 deployments on the bottom of deeper water bodies. In addition, the system could be attached to an unmanned or autonomous  
666 underwater vehicle to allow observations to be made at various depths in the water column in lakes and oceans.

667

668 **Code and data availability**

669 Part of the meteorological data used to carry out heat flux analysis were obtained from Alberta Climate Information Service  
670 (ACIS) <http://agriculture.alberta.ca/acis/weather-data-viewer.jsp>, Environmental and Climate Change Canada (ECCC)  
671 [https://climate.weather.gc.ca/historical\\_data/search\\_historic\\_data\\_e.html](https://climate.weather.gc.ca/historical_data/search_historic_data_e.html), and University of Calgary Biogeoscience Institute  
672 <https://research.ucalgary.ca/biogeoscience-institute/research/environmental-data>. Historic sediment data for the North  
673 Saskatchewan River at Edmonton and Peace River at Dunvegan Bridge can be accessed from Water Survey of Canada  
674 Historical Hydrometric Data [https://wateroffice.ec.gc.ca/mainmenu/historical\\_data\\_index\\_e.html](https://wateroffice.ec.gc.ca/mainmenu/historical_data_index_e.html). All other data and code  
675 used in this study are available from the authors upon request.

676 **Author contribution**

677 CP and JY prepared the apparatus and performed the field work together with advice from YS and ML. CP carried out the  
678 analysis and processing of the data, prepared the figures, and wrote the manuscript with review and contributions from JY,  
679 YS, and ML.

680 **Competing interests**

681 The authors declare that they have no conflict of interest.

682 **Acknowledgements**

683 This research was supported by the Natural Sciences and Engineering Research Council of Canada (NSERC) (Grant nos.  
684 RGPIN-2021-02887, RGPAS-2021-00022 and RGPIN 2020-04358). We would like to thank Heyu Fang, Xun Hong, and  
685 Vincent McFarlane for their assistance in field deployments. We would also like to thank Perry Fedun for providing technical  
686 assistance. The first and second authors are partially funded by the China Scholarship Council (CSC) and the University of  
687 Alberta, respectively. Both are gratefully acknowledged. The map shown in this paper was produced with QGIS software  
688 (<https://qgis.org/en/site/>) using the data provided by © OpenStreetMap contributors  
689 (<https://www.openstreetmap.org/copyright>) and MapTiler (<http://openmaptiles.org/>).

690 **References**

691 Alberta Agriculture and Irrigation, Alberta Climate Information Service (ACIS) Current and Historical Alberta Weather  
692 Station Data Viewer, Available from: <http://agriculture.alberta.ca/acis/weather-data-viewer.jsp>, last access: 28 October 2023.

693 Al-Rousan, T., Masad, E., Tutumluer, E., and Pan, T.: Evaluation of image analysis techniques for quantifying aggregate  
694 shape characteristics, *Constr. Build. Mater.*, 21(5), 978-990, <https://doi.org/10.1016/j.conbuildmat.2006.03.005>, 2007.

695 ~~Arakawa, K.: Studies on the Freezing of Water (II): Formation of Disc Crystals, *Journal of the Faculty of Science, Hokkaido*  
696 *University, Japan*, 2(4), 311-349, 1954.~~

697 Ashton, G.D.: Chapter 2 – Thermal Processes, in: *River Ice Formation*, edited by: Beltaos, S., Committee on River Ice  
698 Processes and the Environment, Edmonton, Alberta, Canada, 19–76, 2013.

699 Barrette, P. D.: Understanding frazil ice: The contribution of laboratory studies, *Cold Reg. Sci. Technol.*, 189, 103334,  
700 <https://doi.org/10.1016/j.coldregions.2021.103334>, 2021.

701 Beltaos, S.: *River ice formation*, edited by: Beltaos, S., Committee on River Ice Processes and the Environment, Canadian  
702 Geophysical Union, Hydrology Section, Edmonton, Alberta, Canada, 2013.

703 Blackburn, J., and She, Y.: A comprehensive public-domain river ice process model and its application to a complex natural  
704 river, *Cold Reg. Sci. Technol.*, 163, 44-58, <https://doi.org/10.1016/j.coldregions.2019.04.010>, 2019.

705 Boyd, S., Ghobrial, T., and Loewen, M.: Analysis of the surface energy budget during supercooling in rivers, *Cold Reg. Sci.*  
706 *Technol.*, 205, 103693, <https://doi.org/10.1016/j.coldregions.2022.103693>, 2023.

707 Clark, S., and Doering, J. C.: Laboratory observations of frazil ice, in: *Proceedings of the 16<sup>th</sup> IAHR International Symposium*  
708 *on Ice (Dunedin, 2002)*, Dunedin, New Zealand, 2-6 December 2002, 2002.

709 Clark, S. P., and Doering, J. C.: Frazil flocculation and secondary nucleation in a counterrotating flume, *Cold Reg. Sci.*  
710 *Technol.*, 55(2), 221-229, <https://doi.org/10.1016/j.coldregions.2008.04.002>, 2009.

711 Clark, S., and Doering, J.: Laboratory experiments on frazil-size characteristics in a counterrotating flume, *J. Hydraul. Eng.*,  
712 132(1), 94-101, [https://doi.org/10.1061/\(asce\)0733-9429\(2006\)132:1\(94\)](https://doi.org/10.1061/(asce)0733-9429(2006)132:1(94)), 2006.

713 ~~Clark, S., and Doering, J.: *Experimental investigation of the effects of turbulence intensity on frazil ice characteristics, Can. J.*  
714 *Civ. Eng.*, 35, 67-79, <https://doi.org/10.1139/L07-086>, 2008.~~

715 Daly, S. F., and Colbeck, S. C.: Frazil ice measurements in CRREL's flume facility, in: *Proceedings of the 8th IAHR*  
716 *International Symposium on Ice (Iowa 1986)*, International Association for Hydraulic Research, Iowa City, Iowa, USA, 18-22  
717 August 1986, 427–438, 1986.

718 Ettema, R., and Zabilansky, L.: Ice influences on channel stability: Insights from Missouri's Fort Peck reach, *J. Hydraul. Eng.*,  
719 130(4), 279-292, [https://doi.org/10.1061/\(asce\)0733-9429\(2004\)130:4\(279\)](https://doi.org/10.1061/(asce)0733-9429(2004)130:4(279)), 2004.

720 Evans, T. W., Margolis, G., and Sarofim, A. F.: Mechanisms of secondary nucleation in agitated crystallizers, *AIChE J.*, 20(5),  
721 950-958, <https://doi.org/10.1002/aic.690200516>, 1974.

722 Ghobrial, T., Pierre, A., Boyd, S., and Loewen, M.: Ice accumulation at a water intake: a case study on the Mille-Iles River,  
723 Québec, *Can. J. Civ. Eng.*, 51(2), 162-173, <https://doi.org/10.1139/cjce-2023-0076>, 2024.

724 Government of Alberta, Alberta Environment and Protected Areas - Alberta River Basins: Lower Kananaskis Lake, ~~Available~~  
725 ~~from:~~ <https://rivers.alberta.ca>, last access: 25 October 2023.

726 Hallett, J.: Crystal growth and the formation of spikes in the surface of supercooled water, *J. Glaciol.*, 3(28), 698-704,  
727 <https://doi.org/10.3189/S0022143000017998>, 1960.

728 Hicks, F.: *An Introduction to River Ice Engineering for Civil Engineers and Geoscientists*, CreateSpace, 2016.

729 Howley, R.: *A modelling study of complex river ice processes in an urban reach of the North Saskatchewan River*, M.Sc.  
730 thesis, University of Alberta, ~~Edmonton~~, Canada, 2021.

731 Jasek, M. and Pryse-Phillips, A.: Influence of the proposed Site C hydroelectric project on the ice regime of the Peace River,  
732 *Can. J. Civ. Eng.*, 42 (9), 645–655, <https://doi.org/10.1139/cjce-2014-0425>, 2015.

733 [Kallungal, J. P. and Barduhn, A. J.: Growth rate of an ice crystal in subcooled pure water, \*AIChE J.\*, 23, 294–303,  
734 <https://doi.org/10.1002/aic.690230312>, 1977.](https://doi.org/10.1002/aic.690230312)

735 Kellerhals, R., Neill, C.R. and Bray, D.I.: *Hydraulic and Geomorphic Characteristics of Rivers in Alberta*, Alberta  
736 Cooperative Research Program in Highway and River Engineering, Edmonton, AB, Canada, 1972.

737 Kempema, E. W., Reimnitz, E., Clayton Jr, J. R. and Payne, J. R.: Interactions of frazil and anchor ice with sedimentary  
738 particles in a flume, *Cold Reg. Sci. Technol.*, 21(2), 137-149, [http://dx.doi.org/10.1016/0165-232x\(93\)90003-g](http://dx.doi.org/10.1016/0165-232x(93)90003-g), 1993.

739 Konzelmann, T., van de Wal, R.S.W., Greuell, W., Bintanja, R., Henneken, E.A.C. and Abe-Ouchi, A.: Parameterization of  
740 global and longwave incoming radiation for the Greenland Ice Sheet, *Global Planet. Change*, 9(1-2), 143-164,  
741 [http://dx.doi.org/10.1016/0921-8181\(94\)90013-2](http://dx.doi.org/10.1016/0921-8181(94)90013-2), 1994.

742 Marko, J.R. and Jasek, M.: Sonar detection and measurement of ice in a freezing river II: Observations and results on frazil  
743 ice, *Cold Reg. Sci. Technol.*, 63(3), 135-153, <https://doi.org/10.1016/j.coldregions.2010.05.003>, 2010.

744 Masad, E., Olcott, D., White, T. and Tashman, L.: Correlation of fine aggregate imaging shape indices with asphalt mixture  
745 performance, *Transportation Research Record: Journal of the Transportation Research Board*, 1757(1), 148–156,  
746 <https://doi.org/10.3141/1757-17>, 2001.

747 McFarlane, V. and Clark, S.P.: A detailed energy budget analysis of river supercooling and the importance of accurately  
748 quantifying net radiation to predict ice formation, *Hydrol. Processes*, 35(3), e14056, <https://doi.org/10.1002/hyp.14056>, 2021.

749 McFarlane, V., Loewen, M. and Hicks, F.: Laboratory measurements of the rise velocity of frazil ice particles, *Cold Reg. Sci.*  
750 *Technol.*, 106, 120-130, <https://doi.org/10.1016/j.coldregions.2014.06.009>, 2014.

751 McFarlane, V., Loewen, M. and Hicks, F.: Measurements of the evolution of frazil ice particle size distributions, *Cold Reg.*  
752 *Sci. Technol.*, 120, 45-55, <https://doi.org/10.1016/j.coldregions.2015.09.001>, 2015.

753 McFarlane, V., Loewen, M. and Hicks, F.: Measurements of the size distribution of frazil ice particles in three Alberta rivers,  
754 *Cold Reg. Sci. Technol.*, 142, 100–117, <https://doi.org/10.1016/j.coldregions.2017.08.001>, 2017.

755 McFarlane, V., Loewen, M. and Hicks, F.: Field measurements of suspended frazil ice. Part I: A support vector machine  
756 learning algorithm to identify frazil ice particles, *Cold Reg. Sci. Technol.*, 165, 102812,  
757 <https://doi.org/10.1016/j.coldregions.2019.102812>, 2019a.

758 McFarlane, V., Loewen, M. and Hicks, F.: Field measurements of suspended frazil ice. Part II: Observations and analyses of  
759 frazil ice properties during the principal and residual supercooling phases, *Cold Reg. Sci. Technol.*, 165, 102796,  
760 <https://doi.org/10.1016/j.coldregions.2019.102796>, 2019b.

761 [Mercier, R. S.: The reactive transport of suspended particles: mechanisms and modeling. Ph.D. thesis, Massachusetts Institute](#)  
762 [of Technology, United States of America, 1985.](#)

763 Morse, B. and Richard, M.: A field study of suspended frazil ice particles, *Cold Reg. Sci. Technol.*, 55(1), 86-102,  
764 <https://doi.org/10.1016/j.coldregions.2008.03.004>, 2009.

765 [Mullins, W. W., and Serkerka, R. F.: Stability of a planar interface during solidification of a dilute binary alloy, J. Appl. Phys.,](#)  
766 [35, 444-451, https://doi.org/10.1063/1.1713333, 1964.](#)

767 Park, C. and Gerard, R.: Hydraulic characteristics of frazil flocs – some preliminary experiments, in: Proceedings of the 7<sup>th</sup>  
768 IAHR International Symposium on Ice, Hamburg, Germany, 27-31 August 1984, 27–35, 1984.

769 Pei, C., She, Y. and Loewen, M.: Laboratory study of frazil ice particle and floc evolution under increased heat flux during  
770 supercooling, in: CGU-HS Committee on River Ice Processes and the Environment (CRIPE) Proceedings of the 22<sup>nd</sup> Workshop  
771 on the Hydraulics of Ice Covered Rivers, Canmore, Canada, 9-12 July 2023, 2023.

772 Pei, C., Yang, J., She, Y. and Loewen, M.: Field measurement of frazil floc properties, in: Proceedings of the 26<sup>th</sup> IAHR  
773 International Symposium on Ice, Montréal, Canada, 19-23 June 2022, 2022.

774 Raphael, J.M.: Prediction of temperature in rivers and reservoirs, *Journal of the Power Division*. 88, 157–181,  
775 <https://doi.org/10.1061/jpweam.0000338>, 1962.

776 [Rees Jones, D. W., and Wells, A. J.: Solidification of a disk-shaped crystal from a weakly supercooled binary melt, Phys. Rev.](#)  
777 [E, 92, 022 406, https://doi.org/10.1103/PhysRevE.92.022406, 2015.](#)

778 Reimnitz, E., Clayton, J. R., Kempema, E. W., Payne, J. R. and Weber, W. S.: Interaction of rising frazil with suspended  
779 particles: tank experiments with applications to nature, *Cold Reg. Sci. Technol.*, 21(2), 117-135, <https://doi.org/10.1016/0165->  
780 [232x\(93\)90002-p](#), 1993.

781 Richard, M., Morse, B., Daly, S.F. and Emond, J.: Quantifying suspended frazil ice using multi-frequency underwater  
782 acoustic devices, *River Res. Appl.*, 27(9), 1106-1117, <https://doi.org/10.1002/rra.1446>, 2011.

783 Rouse, H.: Nomogram for the settling velocity of spheres, in: Division of Geology and Geography, Exhibit D of the Report of  
784 the Commission on Sedimentation, 1936-37, National Research Council, Washington, D.C., 57-64, 1937.

785 Ryan, P., Harleman, D.R. and Stolzenbach, K.D.: Surface heat loss from cooling ponds, *Water Resour. Res.*, 10 (5), 930–  
786 938, <https://doi.org/10.1029/wr010i005p00930>, 1974.

787 Satterlund, D. R.: An improved equation for estimating long-wave radiation from the atmosphere, *Water Resour. Res.*, 15(6),  
788 1649-1650, <https://doi.org/10.1029/wr015i006p01649>, 1979.

789 Schneck, C. C., Laboratory Measurements of the Properties of Frazil Ice Particles and Flocs in Saline Water. M.Sc. thesis,  
790 University of Alberta, Canada, 2018.

791 Schneck, C. C., Ghobrial, T. R., and Loewen, M. R.: Laboratory study of the properties of frazil ice particles and flocs in  
792 water of different salinities, *The Cryosphere*, 13(10), 2751-2769, <https://doi.org/10.5194/tc-13-2751-2019>, 2019.

793 Shen, H. T.: Mathematical modeling of river ice processes, *Cold Reg. Sci. Technol.*, 62(1), 3-13,  
794 <https://doi.org/10.1016/j.coldregions.2010.02.007>, 2010.

795 [Souillé, F., Goeury, C., and Mouradi, R.-S.: Uncertainty analysis of single- and multiple-size-class frazil ice models, \*The\*](#)  
796 [Cryosphere](#), 17, 1645–1674, <https://doi.org/10.5194/tc-17-1645-2023>, 2023.

797 Tsang, G.: Concentration of frazil in flowing water as measured in laboratory and in the field, in: Proceedings of the 7<sup>th</sup> IAHR  
798 International Symposium on Ice, International Association for Hydraulic Research, Hamburg, Germany, 99–111, 1984.

799 University of Calgary, Biogeoscience Institute: Environmental Data, Barrier Lake Field Station Weather Data, ~~Available from:~~  
800 <https://research.ucalgary.ca/biogeoscience-institute/research/environmental-data>, last access: 07 July 2023.

801 Water Survey of Canada, Historical Hydrometric Data: Sediment Data, ~~Available from:~~  
802 [https://wateroffice.ec.gc.ca/mainmenu/historical\\_data\\_index\\_e.html](https://wateroffice.ec.gc.ca/mainmenu/historical_data_index_e.html), last access: 25 October 2023.

803 Yang, J., She, Y., and Loewen, M.: Assessing heat flux formulas used in the full energy budget model for rivers during freeze-  
804 up, in: CGU-HS Committee on River Ice Processes and the Environment (CRIPE) Proceedings of the 22<sup>nd</sup> Workshop on the  
805 Hydraulics of Ice Covered Rivers. Canmore, Canada. 9-12 July 2023, 2023.

806 Ye, S. Q.: A physical and mathematical study of the supercooling process and frazil evolution, Ph.D. thesis, University of  
807 Manitoba, Canada, 2002.